A&A 558, A141 (2013)
DOI: 10.1051/0004-6361/201321979

Astronomy & Astrophysics

X-shooter spectroscopy of young stellar objects

III. Photospheric and chromospheric properties of Class III objects⋆,⋆⋆

B. Stelzer[1], A. Frasca[2], J. M. Alcalá[3], C. F. Manara[4], K. Biazzo[3,2], E. Covino[3], E. Rigliaco[5], L. Testi[4], S. Covino[6], and V. D'Elia[7]

[1] INAF – Osservatorio Astronomico di Palermo, Piazza del Parlamento 1, 90134 Palermo, Italy
e-mail: stelzer@astropa.inaf.it
[2] INAF – Osservatorio Astrofisico di Catania, Via S.Sofia 78, 95123 Catania, Italy
[3] INAF – Osservatorio Astronomico di Capodimonte, Via Moiariello 16, 80131 Napoli, Italy
[4] European Southern Observatory, Karl-Schwarzschild-Str.2, 85748 Garching, Germany
[5] Department of Planetary Science, Lunar and Planetary Lab, University of Arizona, 1629 E. University Blvd, Tucson, AZ 85719, USA
[6] INAF – Osservatorio Astronomico di Brera, Via Bianchi 46, 23807 Merate, Italy
[7] INAF – Osservaotorio Astronomico di Roma, Via di Frascati 33, 00040 Monte Porzio Catone, Italy

Received 28 May 2013 / Accepted 30 July 2013

ABSTRACT

Context. Traditionally, the chromospheres of late-type stars are studied through their strongest emission lines, Hα and Ca II HK emission. Our knowledge on the whole emission line spectrum is more elusive as a result of the limited spectral range and sensitivity of most available spectrographs.
Aims. We intend to reduce this gap with a comprehensive spectroscopic study of the chromospheric emission line spectrum of a sample of non-accreting pre-main sequence stars (Class III sources).
Methods. We analyzed X-shooter/VLT spectra of 24 Class III sources from three nearby star-forming regions (σ Orionis, Lupus III, and TW Hya). We determined the effective temperature, surface gravity, rotational velocity, and radial velocity by comparing the observed spectra with synthetic BT-Settl model spectra. We investigated in detail the emission lines emerging from the stellar chromospheres and combined these data with archival X-ray data to allow for a comparison between chromospheric and coronal emissions.
Results. For some objects in the sample the atmospheric and kinematic parameters are presented here for the first time. The effective temperatures are consistent with those derived for the same stars from an empirical calibration with spectral types. Small differences in the surface gravity found between the stars can be attributed to differences in the average age of the three star-forming regions. The strength of lithium absorption and radial velocities confirm the young age of all but one object in the sample (Sz 94). Both X-ray and Hα luminosity as measured in terms of the bolometric luminosity are independent of the effective temperature for early-M stars but decline toward the end of the spectral M sequence. For the saturated early-M stars the average emission level is almost one dex higher for X-rays than for Hα: $\log(L_{\rm x}/L_{\rm bol}) = -2.85 \pm 0.36$ vs. $\log(L_{\rm H\alpha}/L_{\rm bol}) = -3.72 \pm 0.21$. When all chromospheric emission lines (including the Balmer series up to H11, Ca II HK, the Ca II infrared triplet, and several He I lines) are summed up the coronal flux still dominates that of the chromosphere, typically by a factor 2–5. Flux-flux relations between activity diagnostics that probe different atmospheric layers (from the lower chromosphere to the corona) separate our sample of active pre-main sequence stars from the bulk of field M dwarfs studied in the literature. Flux ratios between individual optical emission lines show a smooth dependence on the effective temperature. The Balmer decrements can roughly be reproduced by an NLTE radiative transfer model devised for another young star of similar age. Future, more complete chromospheric model grids can be tested against this data set.

Key words. stars: pre-main sequence – stars: activity – stars: chromospheres – stars: coronae – stars: fundamental parameters

1. Introduction

The optical spectra of late-type stars are characterized by numerous emission lines. These lines are signatures of chromospheric activity that traces the reaction of the stellar atmosphere to the magnetic processes related to the stellar dynamo. For FGK stars the dynamo may be analogous to the one on the Sun, that is, rooted in the interface between radiative core and convective envelope (Parker 1993), but the nature of the dynamo in fully convective M stars is still elusive. In these stars the solar-like $\alpha\Omega$ dynamo may be replaced by turbulent magnetic fields (Durney et al. 1993) or by an α^2 dynamo (Chabrier & Küker 2006). The same arguments hold for M stars on the pre-main sequence (PMS), which also have fully convective interiors and are not expected to drive a solar-like interface dynamo. Nevertheless, observations indicate that PMS stars manifest particularly strong signatures of chromospheric and coronal activity (e.g. Kuhi 1983; Walter 1986). In fact, searching for coronal X-ray emission is a prime method for discovering PMS stars and, more recently, the UV emission from the chromosphere and transition region has been established as an analogous diagnostic for increasing the census of young stars (e.g. Findeisen & Hillenbrand 2010; Shkolnik et al. 2011). Studies of the physics

⋆ Based on observations collected at the Very Large Telescope of the European Southern Observatory under programs 084.C-0269, 085.C-0238, 086.C-0173, 087.C-0244, and 089.C-0143.
⋆⋆ Tables 2–4 are available in electronic form at http://www.aanda.org

of magnetic activity lag behind not least because all manifestations of magnetic activity (X-rays, UV radiation, optical emission lines) – to a lesser or larger extent – present the problem that in PMS stars other processes such as accretion and outflows may be dominating the contribution from magnetic activity. PMS stars in the accreting stage (Class II sources or classical T Tauri stars) have obtained more attention in the literature than non-accreting ones (Class III or weak-line T Tauri stars). A very small number of studies has been dedicated to chromospheric properties of Class III stars (e.g. Montes & Ramsey 1999), and most of them either focused on a multi-wavelength study for an individual star (e.g. Welty & Ramsey 1995; Fernández et al. 2004) or treated a sample of stars, but for a single activity indicator, the Hα line (Scholz et al. 2007).

Hα is, indeed, the most widely studied emission feature in the optical spectra of M stars. In contrast to FGK stars, where the chromospheric contribution of Hα is superposed onto a photospheric absorption profile, Hα has no absorption component according to synthetic model spectra in M dwarfs. This makes it easier to quantify the chromospheric activity. Moreover, limited wavelength coverage of the spectroscopic observations often makes Hα the only available diagnostic for magnetic activity. For these reasons, Hα is the traditional proxy for characterizing the level of magnetic activity on M stars. However, studies of activity in other wavelength bands, such as Ca II H&K emission, UV and X-ray flux, have shown substantial emission in these activity signatures even in M dwarfs without Hα emission (e.g. Walkowicz et al. 2008; Houdebine 2011). A comprehensive assessment of the chromospheric radiation budget, therefore, requires a study of multiple activity diagnostics.

An ideal instrument for this purpose is the X-shooter spectrograph of the Very Large Telescope at the European Southern Observatory. With its wavelength coverage from 3500−25 000 Å, it includes the whole Balmer series, the calcium H&K and infrared triplet (IRT) lines, several helium lines and the low-n lines of the Paschen and Brackett series. The various diagnostics for magnetic activity trace different layers of the outer atmospheres. The Ca II H&K and IRT line cores originate in the low/middle chromosphere, while the Hα line carries information about upper layers, on average, although it forms in a wide atmospheric thickness (see e.g. Vernazza et al. 1981; Rutten 2007). The He I lines are diagnostics of the upper chromosphere and lower transition region, since the corresponding transitions require temperatures $\geq$10 000 K to be excited. The investigation of atmospheric structure can be expanded into the corona by means of X-ray observations (e.g. Vaiana & Sciortino 1987).

Here we present X-shooter spectra of 24 Class III PMS stars and X-ray data from ROSAT and *XMM-Newton* catalogs for the same stars. The Class III status of this sample was established on the basis of their spectral energy distribution and implies that they are diskless and non-accreting such that the only process responsible for their line emission is magnetic activity. The main purpose of this work is to examine the relations between the emissions in the different lines to constrain the role of activity in the different atmospheric layers. Moreover, we aim at constraining the dependence of the activity level on fundamental properties such as effective temperature ($T_{\rm eff}$), bolometric luminosity ($L_{\rm bol}$), rotation, and age, parameters that determine the nature of stellar dynamos. The radiation produced through magnetic processes is known to be linked to the stellar bolometric luminosity and is often normalized to it by defining the "activity index", $L_{\rm proxy}/L_{\rm bol}$, where $L_{\rm proxy}$ is the luminosity of an emission line or a wavelength band (e.g. in the case of X-ray emission). Our sample spans the whole spectral M sequence and gives natural access to examining the role of $T_{\rm eff}$ from 2500 to 4500 K. Bolometric luminosity, effective temperature, rotation rate ($v \sin i$), surface gravity, and lithium absorption are all determined using the same X-shooter spectra as those in which we measured the activity diagnostics, which yields a self-consistent picture of photospheric and chromospheric properties of Class III sources to which we add the coronal perspective using archived X-ray data. Finally, we compare the results to chromospheric and coronal studies of main-sequence M dwarfs from the literature to search for keys on the time evolution of magnetic activity.

In Sect. 2 we give more details on the sample and the data used. The determination of fundamental parameters, rotation, kinematics, and lithium absorption and the analysis of the emission lines are described in Sect. 3. The results on magnetic activity are presented in Sect. 4, and a summary and our conclusions are found in Sect. 5.

2. Sample and observations

The sample considered in this paper comprises 24 Class III objects, 13 from the TW Hya association (henceforth TWA), 6 from the Lupus III, and 5 from the σ Orionis star-forming regions (SFRs). All stars were observed with X-shooter within the INAF consortium's guaranteed time observations (GTO; see Alcalá et al. 2011, for a presentation of the project). The target list is given in Table 1. The coordinates and other designations for the objects are found in Table 1 of Manara et al. (2013, henceforth MTR 13), where the same sample and the data reduction are described in detail. We provide here only a short summary.

The classification as Class III sources was derived using published *Spitzer* photometry and spectroscopic features. In particular, we made use of the slopes of the spectral energy distribution (SEDs) determined by Merín et al. (2008) for Lupus and by Hernández et al. (2007) for σ Ori members. Because the mid- and far-IR SEDs are not available or incomplete for most stars in the TWA, we have used for these stars the Hα equivalent width criterion defined by White & Basri (2003) and the absence of forbidden emission lines in our X-shooter spectra. The Hα and the forbidden lines were also used to confirm the Class III status of the objects in Lupus and σ Ori.

2.1. X-shooter spectra

The X-shooter observations were carried out between May 2010 and April 2012. Individual exposure times and slit widths were chosen depending on the brightness of the star (see Table 2 of MTR 13). Briefly, the exposure times ranged from 100 s to 3600 s, and the slit widths yielded spectral resolutions ranging from $R \sim$ 3300...9100 in the UVB, $R \sim$ 5400...17 400 in the VIS, and $R \sim$ 3500...11 300 in the near-infrared (NIR). The data reduction was performed with the X-shooter pipeline (Modigliani et al. 2010). Finally, the flux-calibrated spectrum was scaled by an individual factor for each star to adapt it to the published broad-band photometry. In this way, eventual slit losses and non-photometric conditions were compensated for.

MTR 13 have defined a spectral sequence for this sample of Class III objects by ordering the stars according to the depth of molecular features. Some widely used spectral indices were shown to be consistent with this scale. In Table 1 we report some parameters derived and/or compiled by MTR 13 that are useful for our analysis: the spectral types (SpT), the bolometric

Table 1. Fundamental and atmospheric parameters, rotation, and kinematics of Class III sample.

Name	SpT[†]	$\log \frac{L_{\rm bol}}{L_\odot}$[†]	d[†] [pc]	$P_{\rm rot}$[‡] [d]	$T_{\rm eff}$ [K]	$\log g$ [cm/s^2]	R_* [$R_\odot$]	$v \sin i$ [km s^{-1}]	RV [km s^{-1}]	$W_{\rm Li}$ [mÅ]
TWA 9A	K5	−0.61	68	5.10	4333 ± 47	4.9 ± 0.8	0.87	14.2 ± 0.4	11.7 ± 0.4	498 ± 53
SO 879	K7	−0.29	360	...	4021 ± 85	3.9 ± 0.5	1.47	10.0 ± 4.0	35.0 ± 1.3	599 ± 66
TWA 6	K7	−0.96	51	0.54	4020 ± 173	4.8 ± 0.5	0.68	76.8 ± 1.3	17.1 ± 1.5	485 ± 54
TWA 25	M0	−0.61	54	...	3749 ± 60	4.7 ± 0.5	1.17	14.4 ± 0.5	8.8 ± 1.2	549 ± 58
TWA 14	M0.5	−0.83	96	0.63	3756 ± 99	4.7 ± 0.6	0.90	46.0 ± 0.7	14.9 ± 1.3	577 ± 59
TWA 13B	M1	−0.70	59	5.35	3661 ± 103	4.6 ± 0.6	1.10	10.4 ± 1.1	11.2 ± 0.7	526 ± 57
TWA 13A	M1	−0.61	59	5.56	3616 ± 87	4.8 ± 0.5	1.25	10.0 ± 0.7	10.0 ± 1.0	595 ± 65
TWA 2A	M2	−0.48	47	...	3533 ± 133	4.4 ± 0.4	1.53	18.0 ± 1.9	10.0 ± 1.1	536 ± 63
Sz 122[*]	M2	−0.60	200	...	3494 ± 126	4.6 ± 0.5	1.36	150.2 ± 2.7	18.1 ± 3.0	268 ± 54
TWA 9B	M3	−1.17	68	3.98	3357 ± 67	4.5 ± 0.6	0.76	11.6 ± 2.2	11.0 ± 0.5	476 ± 57
TWA 15B	M3	−0.96	111	0.72	3463 ± 129	4.6 ± 0.6	0.91	21.6 ± 0.9	11.8 ± 1.2	477 ± 65
TWA 7	M3	−1.14	28	5.05	3408 ± 85	4.4 ± 0.4	0.77	8.4 ± 1.3	8.4 ± 0.8	551 ± 64
TWA 15A	M3.5	−0.95	111	0.65	3347 ± 125	4.5 ± 0.3	0.99	33.6 ± 0.9	10.1 ± 1.7	542 ± 62
Sz 121[*]	M4	−0.34	200	...	3286 ± 134	4.1 ± 0.3	2.07	84.8 ± 3.3	13.6 ± 2.5	575 ± 68
Sz 94	M4	−0.76	200	...	3219 ± 101	4.3 ± 0.3	1.33	29.8 ± 2.7	6.4 ± 2.6	...
SO 797	M4.5	−1.26	360	...	3274 ± 136	3.9 ± 0.4	0.72	27.4 ± 0.9	32.0 ± 2.0	548 ± 67
SO 641	M5	−1.53	360	1.75	3176 ± 140	3.8 ± 0.4	0.56	12.5 ± 4.9	29.5 ± 3.8	554 ± 69
Par-Lup3-2	M5	−0.75	200	...	3038 ± 101	3.7 ± 0.4	1.51	26.4 ± 4.7	4.4 ± 3.7	575 ± 72
SO 925	M5.5	−1.59	360	1.79	3113 ± 178	3.8 ± 0.4	0.55	20.8 ± 4.2	31.7 ± 4.4	530 ± 78
SO 999	M5.5	−1.28	360	0.95	3047 ± 131	3.8 ± 0.4	0.82	16.3 ± 4.0	31.2 ± 2.0	593 ± 84
Sz 107	M5.5	−0.79	200	...	3045 ± 111	3.7 ± 0.3	1.44	72.5 ± 3.3	3.6 ± 4.8	532 ± 89
Par-Lup3-1	M6.5	−1.18	200	...	2860 ± 106	3.6 ± 0.4	1.04	19.0 ± 2.0	4.9 ± 4.4	529 ± 177
TWA 26	M9	−2.70	42	...	2476 ± 109	3.6 ± 0.5	0.24	34.9 ± 14.3	5.2 ± 9.8	578 ± 99
TWA 29	M9.5	−2.81	79	...	2390 ± 109	3.6 ± 0.3	0.23	35.8 ± 17.2	7.7 ± 3.9	590 ± 133

Notes. [(*)] Fundamental and kinematic parameters of Sz 121 and Sz 122 are uncertain due to possible binarity. [(†)] Spectral type, bolometric luminosity and distance adopted from MTR 13. [(‡)] Rotation periods from Lawson & Crause (2005) for TWA members and from Cody & Hillenbrand (2010) for σ Ori members.

luminosities ($L_{\rm bol}$), and the distances (d). We also give the values for the photometric rotation periods from the literature ($P_{\rm rot}$).

An essential part throughout this study is the analysis of spectral lines, and we anticipate here the treatment of the uncertainties of the line fluxes. We considered them to be composed of two components, the statistical measurement error and a systematic error associated with the flux calibration. As mentioned above, MTR 13 have normalized the spectra to published photometry such that the error in the flux eventually traces the uncertainties of the photometric measurements and especially the variations due to magnetic activity which we assumed to be 10%. (We note that the multi-band photometry of our objects is not contemporaneous.) The two uncertainties (statistical and systematic) are summed quadratically.

2.2. Ancillary X-ray data

We have collected X-ray data from the literature and from public data archives. The flux measured at Earth is given for all stars in Table 2 and was obtained in the following way.

In a first step, we cross-correlated the target list with the Bright Source Catalog (BSC; Voges et al. 1999) and with the Faint Source Catalog (FSC; Voges et al. 2000) of the ROSAT All-Sky Survey (RASS). We used a match radius of 40″ (e.g. Neuhäuser et al. 1995). We found that 11 stars are identified with a BSC X-ray source and one is detected in the FSC. To obtain X-ray fluxes for the other half of our sample we searched the literature. For the stars in σ Ori and Lupus we made use of the *XMM-Newton* measurements published by Franciosini et al. (2006) and Gondoin (2006), respectively. Four of the six Class III objects in Lupus and two of the five in σ Ori are listed as X-ray sources in these works. The TWA covers a large area on the sky and no dedicated *XMM-Newton* or *Chandra* observations have been performed to study its stellar population. We note that 11 of the 12 RASS identifications are objects from the TWA. The two brown dwarfs (BDs), TWA 26 and TWA 29, are not detected in the RASS but their X-ray emission has been studied by Castro et al. (2011) and Stelzer et al. (2007) on the basis of a dedicated *Chandra* and a serendipitous *XMM-Newton* observation, respectively. TWA 29 was not detected and an upper limit was given by Stelzer et al. (2007). For the remaining four targets without X-ray detection we assumed an upper limit to the RASS count rate of 0.02 cts/s, corresponding to the sensitivity limit for a typical RASS exposure time of ≈400−500 s (see Stelzer et al. 2013). The matches and table handling was carried out in the Virtual Observatory environment TOPCAT (Taylor 2005) and in IDL[1].

We transformed the RASS count rates and upper limits into 0.12−2.5 keV flux assuming a thermal model with plasma temperature of kT = 1 keV and an absorbing column density of $N_{\rm H} = 10^{20}$ cm^{-2}. Then, X-ray luminosities were calculated using the individual distances from Table 1. For the stars with X-ray data in the literature the published X-ray luminosities can be used. However, to make them comparable with those from the RASS, two corrections had to be applied. The first one is a transformation from the *XMM-Newton* and *Chandra* energy bands for which the luminosities had been calculated to the energy band of ROSAT. The correction factors for the literature sources are between 0.99 and 1.38. The published X-ray luminosities were multiplied by these factors. Moreover, they were

[1] The Interactive Data Language (IDL) is a registered trademark of ITT Visual Information Solutions.

corrected for the differences in the distances adopted in the literature and by us.

We added a 10% systematic error to the statistical errors of all X-ray measurements. The lower and upper values for the X-ray flux corresponding to the uncertainties are given in brackets in Table 2.

3. Analysis

3.1. Stellar parameters and rotation determined with ROTFIT

We used the ROTFIT code (Frasca et al. 2006) for evaluating the atmospheric parameters, effective temperature ($T_{\rm eff}$) and surface gravity ($\log g$), and for determining the projected rotation velocity ($v \sin i$). For this purpose, we adopted as templates a grid of synthetic BT-Settl spectra (Allard et al. 2012) with solar metallicity, effective temperature in the range 2300−4400 K (in steps of 100 K) and $\log g$ from 5.5 to 3.0 (in steps of 0.5). The synthetic spectra were degraded in resolution to match that of the target spectra, which depends on the adopted slit width, and they were resampled on their spectral points. For each target spectrum, ROTFIT sorts the synthetic templates according to the χ^2 of the residuals "observed − template", where the synthetic templates are progressively broadened by convolution with a rotational profile of increasing $v \sin i$ until a minimum χ^2 is reached. The stellar parameters adopted by us are averages of the values of the five best templates (for each of the analyzed spectral regions described in detail below) weighted according to the χ^2. The standard error of the weighted mean was adopted as the measurement error. By using the five best-fitting models instead of the one best fit we achieve a higher accuracy because of the coarse sampling of the stellar parameters in the grid of templates. The weighted average with a larger number of model spectra (e.g. ten) does not change significantly since the χ^2 increases quite rapidly after the first five models, lowering their weight.

The analysis is based on the assumption of negligible extinction in our targets. In fact, the three SFRs observed during our X-shooter survey were chosen, amongst others, because their low extinction yields a high signal in the UVB range where very low-mass YSOs are intrinsically faint. Individual values for the optical extinction, A_V, of Lupus members can be found in Hughes et al. (1994) and Comerón et al. (2003). For all but one object of our Lupus sample $A_V = 0$ mag. For the low reddening of the σ Ori cluster see for instance the references in Walter et al. (2008). Finally, the TWA is a nearby young association with negligible extinction because it is located far from molecular clouds.

The derived values for $T_{\rm eff}$, $\log g$ and $v \sin i$ are given in Table 1. We also list the stellar radii (R_*) computed from the effective temperatures and the bolometric luminosities with the Stefan-Boltzmann law.

3.1.1. Spectral regions for ROTFIT analysis

The best spectral regions for performing an accurate determination of $v \sin i$ with ROTFIT are those free of very broad lines and strong molecular bands, but including several absorption lines strong enough to still be prominent features against a well-defined continuum in fast rotators as well. We found a very well-suited region between 9600 and 9800 Å where several sharp absorption lines (mainly of Ti I and Cr I) are present (cf. Fig. 1) for stars hotter than 2900 K. Moreover, the intensity of these lines scales with $T_{\rm eff}$ as apparent from the BT-Settl models, thus they can be also used as temperature diagnostics. We derived the $v \sin i$ as the weighted mean described above using only this spectral region and kept it fixed inside ROTFIT to determinate the atmospheric parameters based on other spectral diagnostics.

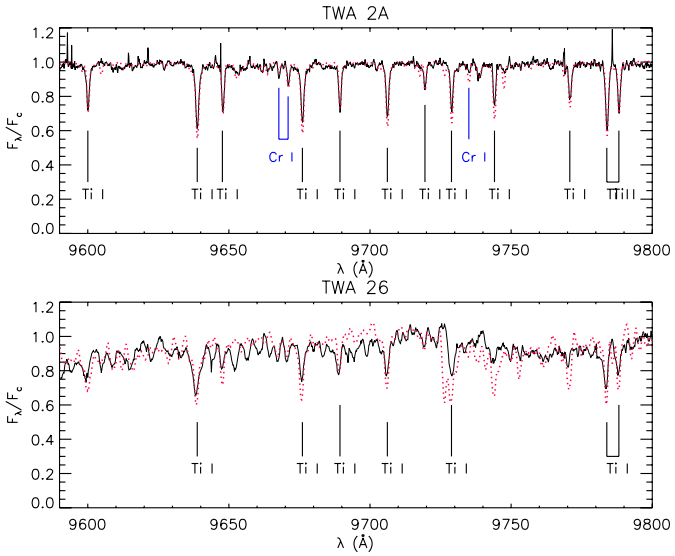

Fig. 1. Portion of continuum-normalized X-shooter VIS spectra of TWA 2A (*top panel*) and TWA 26 (*lower panel*) around 9700 Å (solid black lines). The best-fitting synthetic spectra, properly Doppler-shifted and rotationally broadened, are overplotted (dotted red lines). The main absorption lines are also marked.

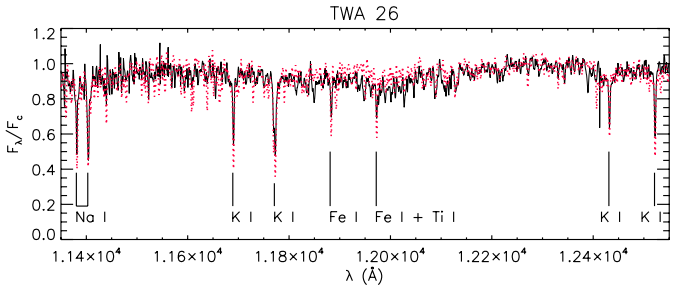

Fig. 2. Portion of the X-shooter NIR spectrum of TWA 26 around 12 000 Å (solid black line) and the best fitting synthetic spectrum (dotted red line).

The spectral region around 9700 Å of the two coolest objects in our sample, TWA 26 and TWA 29, is much more affected by molecular bands and noise than that of the hotter stars, and the Ti I absorption lines become quite faint (see Fig. 1). Thus we used another spectral region as temperature diagnostics, the wavelength range 11 300−12 600 Å in the NIR spectra, where several absorption lines are visible (cf. Fig. 2). Unfortunately, the resolution and sampling of the NIR spectra is lower than that of the VIS spectra, which makes the $v \sin i$ determinations less accurate.

To determinate the surface gravity we selected three additional spectral regions that contain the Na I doublet at $\lambda \approx$ 8190 Å, the K I doublet at $\lambda \approx$ 7660−7700 Å, and a spectral segment from 7020 to 7150 Å that contains three TiO molecular bands sensitive to both gravity and temperature. In Fig. 3 we display an example of the result of the fit performed by ROTFIT in these three regions. As for the $v \sin i$ region, the observed and template spectra were scaled one over the other by means of continuum (or pseudo-continuum) windows close to the analyzed spectral diagnostics. The adopted value of $\log g$ is the weighted

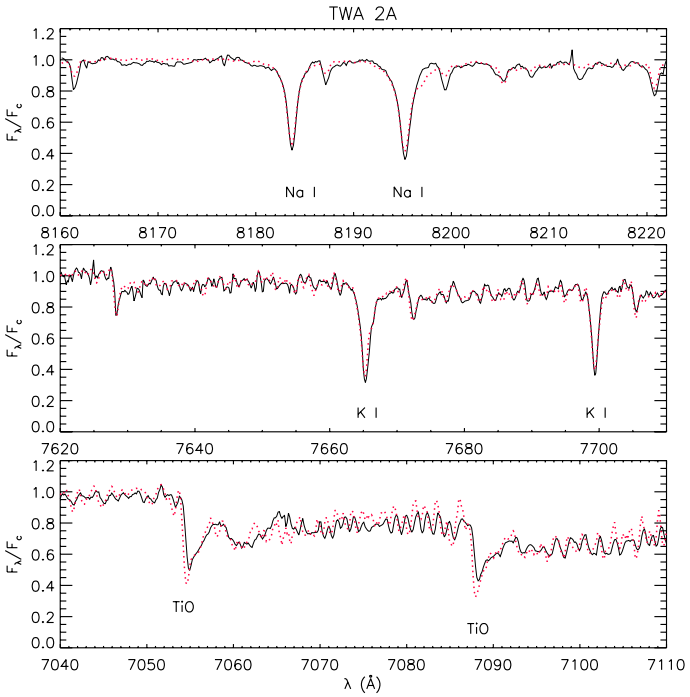

Fig. 3. Observed (solid black lines) and fitted synthetic spectrum (dotted red lines) of TWA 2A in the three spectral regions chosen to determine the atmospheric parameters with ROTFIT. The most prominent absorption features are labeled.

average again made with the five best templates for each of these three regions. For $T_{\rm eff}$ we also included in the average the results of the analysis of the spectral segment around 9700 Å, which contains several lines whose intensity depends on the temperature, but we excluded the Na I doublet, which has a very strong dependency on $\log g$ that can mask the lower sensibility to $T_{\rm eff}$.

3.1.2. Results and comparison with the literature

The left panel of Fig. 4 demonstrates that the effective temperatures agree excellently with those of MTR 13. They obtained the temperatures from the spectral types using the conversion presented by Luhman et al. (2003), and this empirical temperature scale is here confirmed throughout the whole M spectral sequence. The derived surface gravities range from $\log g \approx 3.6$ to ≈4.9 for our targets. With the exception of the two coolest objects, the two BDs TWA 26 and TWA 29, all stars in the TWA have systematically higher gravities than those in Lupus and σ Ori, which is qualitatively consistent with the canonical age difference between the three SFRs (right panel of Fig. 4). The 1, 10, and 100 Myr isochrones of the PMS evolutionary models from Baraffe et al. (1998) and Chabrier et al. (2000) are overplotted on the $\log g$ vs. $T_{\rm eff}$ diagram. "NEXTGEN" and "DUSTY" models are joined here at 3000 K. The gravities that we derived for the M stars in the TWA are systematically higher than predicted by the models for an age of ∼10−15 Myr, although the effect is only marginal considering the uncertainties. For the two BDs we confirm the similar result of Mohanty et al. (2004), who found lower gravities than predicted by the Baraffe et al. (1998) and Chabrier et al. (2000) models for a sample of BDs in the ≈11 Myr old Upper Sco region (see Pecaut et al. 2012, for a comprehensive discussion of the age of Upper Sco). As a consequence of the low gravity, the BDs appear younger in the HR diagram than the M stars located in the same star-forming environment (see Fig. 6 of MTR 13). In Fig. 4 (right) we have excluded Sz 122 and Sz 121 because their line profiles are dominated by fast rotation and/or binarity and we could not determine reliable values for their gravities. One of the remaining stars in Lupus, Sz 94, has higher gravity than the other objects in the same SFR. This star is later discarded from our sample due to the lack of lithium absorption (see Sect. 3.4).

Sz 122 and Sz 121 are the only two stars from Lupus in our sample with previous $v \sin i$ measurements. Similar to our results, Dubath et al. (1996) have found very high rotation rates for them. These stars are likely spectroscopic binaries, therefore their $v \sin i$ values are uncertain (see also Sect. 3.3). Rotation velocities have previously been presented for ten of the stars in the TWA, and the $v \sin i$ values from the literature agree well with our ROTFIT measurements. No $v \sin i$ are published for our targets in σ Ori.

Photometric measurements of rotation periods ($P_{\rm rot}$) are available for half of our sample (Lawson & Crause 2005; Cody & Hillenbrand 2010) and are listed in Table 1. We have combined these $P_{\rm rot}$ values with our results on $v \sin i$ to compute the lower limit to the stellar radii, $R \sin i$. The values are compatible with the radii $R_{*,\rm SB}$ determined from $L_{\rm bol}$ and $T_{\rm eff}$ within the errors, which consider the uncertainties of $v \sin i$ and the 0.2 dex uncertainty in the bolometric luminosities (see MTR 13).

To summarize, the comparison with previous measurements and with predictions of evolutionary models confirms that we have derived reliable estimates of the atmospheric parameters. This was achieved through a careful selection of the spectral regions in which we carried out the comparison with the model spectra as described in Sect. 3.1.1.

3.2. Stellar radius from the Barnes-Evans relation

We used published photometry of our targets to determine the stellar radii from the empirical relation between angular diameter and surface brightness derived by Barnes & Evans (1976) for giants that was extended to dwarf stars by Beuermann et al. (1999). Specifically, we applied Eq. (6) of Beuermann et al. (1999) to the observed $V - K$ colors after transforming the 2 MASS $K_{\rm s}$ magnitudes to the CIT system with the transformations given by Carpenter (2001). In Fig. 5, the resulting radii are compared with those obtained from the Stefan-Boltzmann law. Four of the five objects that are missing in this figure have no measurement of the V magnitude. The fifth one is TWA 14, for which we found a 50% difference between the radii computed with the two methods. This can be attributed to a problem with the photometry that was previously pointed out by Zuckerman & Song (2004). For all other stars the two values agree within 20%, a remarkable fact given that the calibration of Beuermann et al. (1999) was based on only eight stars and that their sample was comprised of young-disk M dwarfs, while ours is composed of PMS stars with somewhat lower gravity. In Fig. 5 the effect of variable photometry is shown as a vertical bar for stars with more than one measurement in the V band; it shows that the spread produced by variability is likely not relevant. Finally, some uncertainty may result from extinction. Because our stars are relatively nearby (∼50−350 pc) and have no major circumstellar material we did not apply a reddening correction to the photometry. The comparison of the X-shooter spectra to spectral templates (see MTR 13) shows no evidence for reddening within a precision of ∼0.5 mag. Indeed, $A_V \sim 0.3$ mag is sufficient to remove the apparently systematic trend of the stars in Lupus to be located below the 1:1 relation in Fig. 5.

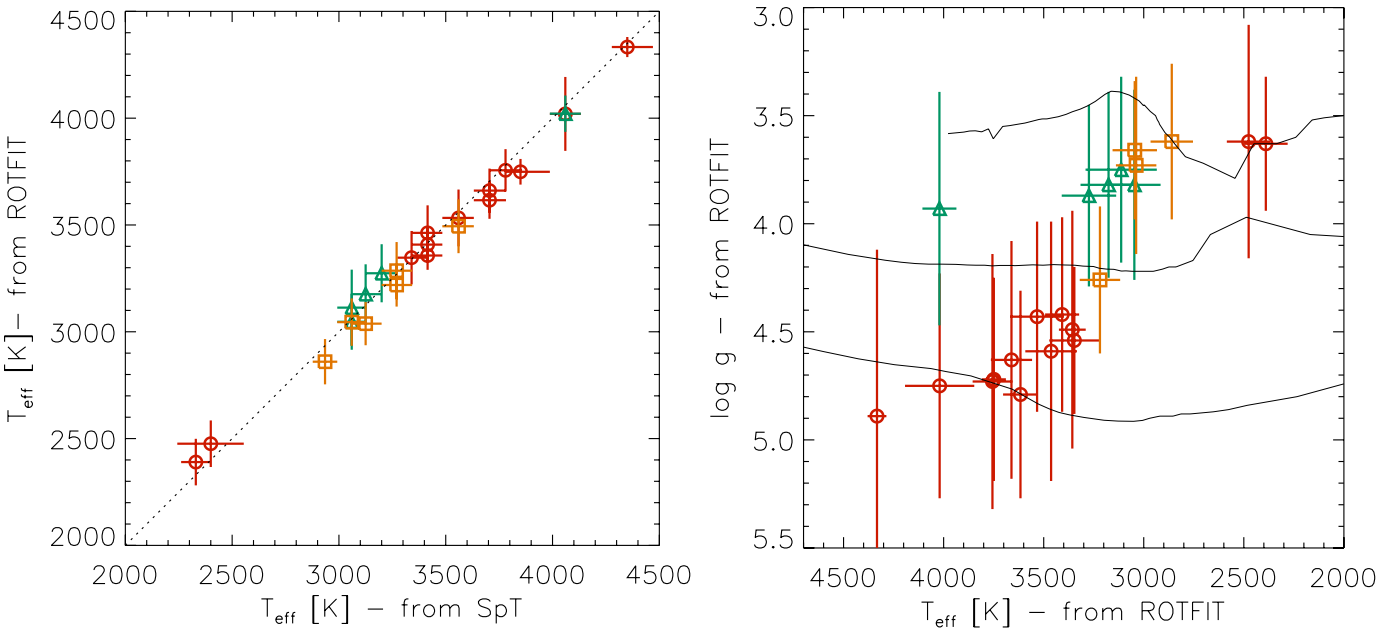

Fig. 4. *Left panel*: comparison between effective temperatures obtained by MTR 13 from the SpT with the temperature scale of Luhman et al. (2003) and those derived here with ROTFIT. *Right panel*: surface gravity vs. effective temperature both derived with ROTFIT and compared with the predictions of evolutionary PMS models by Baraffe et al. (1998) and Chabrier et al. (2000), for which we show as black lines the 1, 10, and 100 Myr isochrones (from top to bottom). Different colors and plotting symbols denote stars from the three SFRs: green triangles – σ Ori, orange squares – Lupus, red circles – TWA. Sz 121 and Sz 122 are excluded from the right panel because their broad lines did not allow us to determine the gravity.

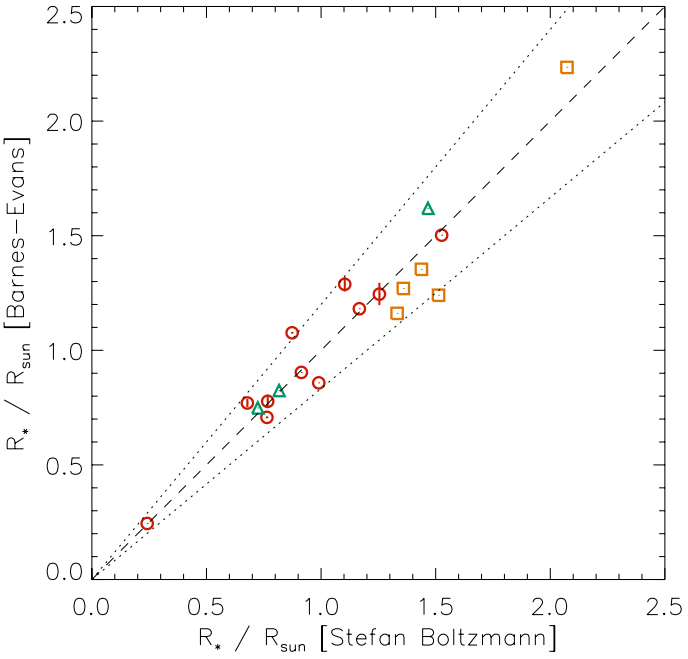

Fig. 5. Comparison of the stellar radii calculated from the Stefan-Boltzmann law and from the Barnes-Evans relation. The 1:1 line is shown as a dashed line and a 20% difference between the two radii is represented as dotted lines. Same plotting symbols as in Fig. 4. Not included in this plot are SO 641, SO 925, Par-Lup3-1, TWA 29, and TWA 14 because they lack the photometry required for the Barnes-Evans relation (see text in Sect. 3.2).

3.3. Radial velocity

We determined the radial velocity (*RV*) of all stars in our sample using the cross-correlation technique. We calculated the cross-correlation function (CCF) between the observed and synthetic spectra within ROTFIT to evaluate the velocity shift to be applied to the latter. The CCF peak was fitted with a Gaussian to determine more accurately its center. The standard error of the weighted mean was adopted as the measurement error for the atmospheric parameters. Despite the poor statistics, it is worth noticing that the *RV* errors tend to be larger for stars with higher $v \sin i$, as expected. The barycentric correction was performed with the IDL procedure BARYVEL. The results of the *RV* determination are given in Table 1.

The radial velocity had previously been measured for all but one of the TWA members in our sample. For most stars our results agree well with the values published in the literature that have been summarized by Schneider et al. (2012). Only for two stars (TWA 7 and TWA 9A) the previous and our new estimates are different by more than 2σ. The *RV* of TWA 29 has been measured for the first time here and its value of $7.7 \pm 3.9\,\mathrm{km\,s^{-1}}$ is consistent with it being a member of the association.

Wichmann et al. (1999) have studied the radial velocities in the Lupus SFR. They distinguished between accreting and non-accreting YSOs in the usual way on the basis of the Hα equivalent width and evaluated the *RV* of these two samples, classical T Tauri stars (CTTS) and weak-line T Tauri stars (WTTS), separately. They showed that the radial velocities of the WTTS are similar to those of the CTTS for the WTTS sample on the clouds ($\langle RV_{\mathrm{CTTS}}\rangle = -0.03 \pm 1.20\,\mathrm{km\,s^{-1}}$; $\langle RV_{\mathrm{WTTS,on}}\rangle = 1.29 \pm 0.87\,\mathrm{km\,s^{-1}}$), while the WTTS outside the clouds clearly have a higher mean radial velocity, $\langle RV_{\mathrm{WTTS,off}}\rangle = 3.17 \pm 1.39\,\mathrm{km\,s^{-1}}$. Considering the uncertainties, the X-shooter Class III sample in Lupus is compatible with the two WTTS populations examined by Wichmann et al. (1999) if we exclude two stars with significantly higher values. The two stars that we excluded from the *RV* average are Sz 121 and Sz 122. Sz 122 is the star with the highest $v \sin i$ ($\approx 150\,\mathrm{km\,s^{-1}}$). Its CCF shows a double-shaped peak that could be the result of Doppler bumps produced by starspots. However, given its very high rotation velocity, we think it is more

likely the fingerprint of binarity. Moreover, the RV values given by Dubath et al. (1996) for Sz 122 and Sz 121 are inconsistent with our results, pointing at variability related to a companion. More observations are needed to confirm the binary nature of these two stars.

For σ Ori, Sacco et al. (2008) studied nearly 100 stars with spectral types K6-M5 and found an *RV* distribution centered on +30.93 km s^{-1} with a standard deviation of 0.92 km s^{-1}. The radial velocities we derived for the X-shooter sample in σ Ori range from +29.5 km s^{-1} to +35.0 km s^{-1} and agree excellently with the mean cluster value within their uncertainties.

3.4. Lithium absorption

The lithium absorption feature at 6708 Å is a widely used youth indicator for low-mass stars because for fully convective stars this element is rapidly depleted during the PMS evolution (Bildsten et al. 1997). As already mentioned by MTR 13, we have detected this Li I line in all stars except for Sz 94. All other properties, for instance the position in the HR diagram, our *RV* measurement and the proper motion given by López Martí et al. (2011), are compatible with Sz 94 being a Lupus member. However, the absence of lithium in such a young PMS star is difficult to explain, and we conclude that this is very likely a foreground object with Lupus-like kinematics by coincidence. In any case, for this study we discarded Sz 94 from our sample.

The lithium equivalent width ($W_{\rm Li}$) was determined within IRAF[2] from a by-eye estimate of the local continuum. The results are given in Table 1. The uncertainties represent the mean and standard deviations from three measurements carried out on the line, to which we have added a 10% systematic error as explained in Sect. 2.1. The $W_{\rm Li}$ of the remaining 23 Class III sources is shown in Fig. 6 as a function of effective temperature. There is no evident trend, that is, the Li I λ6708 Å equivalent width does not depend on effective temperature throughout the whole M spectral class. After excluding Sz 94, all but one star in our sample have values in the range ≈500−600 mÅ. Only Sz 122 has much lower $W_{\rm Li}$. We recall that for this star we observed very broad lines; it may be a binary. The companion may affect our line measurement in a way that is impossible to quantify. Qualitatively, the combination of two spectra could give a very weak lithium absorption if the spectral types of the two components are very different and one of the two stars has weak lithium.

In Fig. 6 the observed equivalent widths are also compared with curves of growth calculated by Zapatero Osorio et al. (2002) and by Palla et al. (2007). Palla et al. (2007) provided the lithium abundance, A(Li), in steps of 0.5, and we show the curves for $\log g = 4.0$ and 4.5. Zapatero Osorio et al. (2002) covered a wider temperature range. We show their results for $\log g = 4.5$ in the range A(Li) between 2.5 and 3.1 as gray shaded. The $\log g$ values of both calculations are close to the gravities we measured for the Class III sample (see also Table 1). The best agreement between the calculations and our measurements is reached for A(Li) ≈ 3.0, indicating that these stars have retained their primordial lithium abundance. This is also suggested by the fact that no difference in $W_{\rm Li}$, and consequently in lithium abundance, is observed in objects belonging to the three SFRs despite their age difference. Finally, we found good agreement with the lithium measurements by Mentuch et al. (2008) for the 11 TWA members that we have in common with their study.

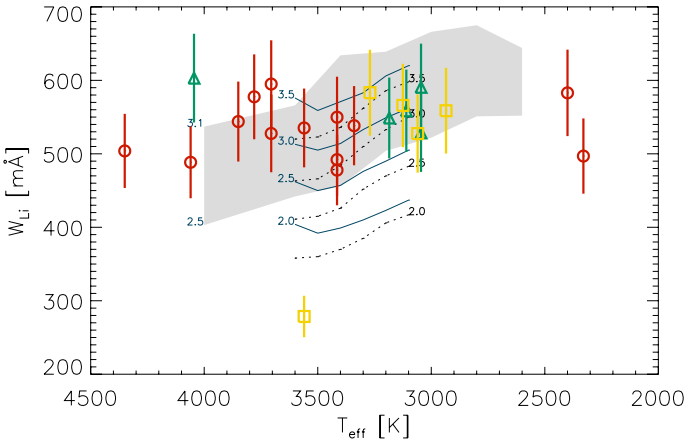

Fig. 6. Lithium equivalent width versus effective temperature. Same plotting symbols as in Fig. 4. For clarity tiny horizontal offsets are applied to the data for σ Ori and Lupus stars. Overplotted are curves of growth from Zapatero Osorio et al. (2002) for $\log g = 4.5$ and a range of A(Li) = 2.5−3.1 as gray shaded and from Palla et al. (2007) for $\log g = 4.0$ (black dotted) and 4.5 (blue solid) and four different abundances between A(Li) = 2.0 and 3.5 as labeled.

3.5. Emission lines

The observed fluxes of the major emission lines in the X-shooter spectra of our sample have been determined by MTR 13. These measurements were obtained by direct integration of the flux above the local continuum. Analogous to the case of the lithium absorption line and as explained in Sect. 2.1, we assumed a 10% systematic error that we added to the statistical measurement errors given by MTR 13.

Generally, accurate line measurements require taking into account the photospheric absorption component of the lines, for example by subtracting a template spectrum from the observed spectrum and calculating the emission line flux from the residual. The template spectrum can be either an observation of an inactive star of the same spectral type (see e.g. Frasca & Catalano 1994; Montes et al. 1995) or a model spectrum. For late-K and M stars, the only emission lines with a significant photospheric absorption component are the three Ca II IRT lines. For these lines we determined the chromospheric emission line fluxes by applying the spectral subtraction technique described below that was previously also adopted by MTR 13. In contrast to that work, we used synthetic spectra with individual parameters ($T_{\rm eff}$, $\log g$ and $v \sin i$) for each star instead of adopting constant gravity and negligible rotation for all objects. For these reasons, we consider our values for these lines more accurate and adopted the new estimates for the subsequent analysis. For all other emission lines we made use of the fluxes measured and published by MTR 13. To analyze the Ca II IRT we adopted the same BT-Settl synthetic spectra as inactive templates for the spectral subtraction that were used to determine the atmospheric parameters.

To check the reliability of the synthetic spectra as inactive templates, we compared them with medium-resolution spectra of three low-mass and low-activity stars, namely 61 CygA (K5 V), 61 CygB (K7 V), and HD1326A (M2 V), retrieved from the Library of Fiber Optic Echelle spectra of F, G, K, and M field dwarfs (Montes et al. 1999). We found that the shape and the residual flux in the cores of Ca II IRT lines is nearly the same

[2] IRAF is distributed by the National Optical Astronomy Observatories, which are operated by the Association of Universities for Research in Astronomy, Inc., under cooperative agreement with the National Science Foundation.

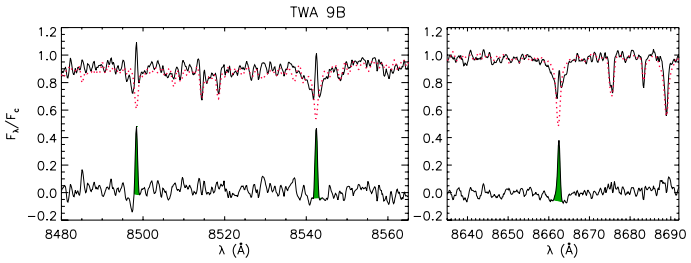

Fig. 7. Example of the spectral subtraction procedure. The synthetic inactive template (dotted red line) is overplotted on the observed continuum-normalized spectrum of TWA 9B (solid black line). The differences between observed and template spectra are plotted at the bottom of each box. The hatched areas in the difference spectra represent the excess emissions that have been integrated to obtain the net equivalent widths of the Ca II IRT lines.

for these low-activity stars and synthetic spectra, which justifies the use of the synthetic spectra as inactive templates.

To derive the proper surface flux at the continuum corresponding to the $T_{\rm eff}$ value listed in Table 1, we interpolated the BT-Settl spectra to this temperature. The mean continuum flux in the range 8570−8640 Å was evaluated both in the target spectrum and in the template. This enabled us to set both spectra on the same scale of continuum-normalized flux for the subtraction and convert the net equivalent width ($W_i^{\rm em}$) of each line i, measured integrating the residual spectrum, into flux at the stellar surface ($F_{{\rm surf},i}$) by simply multiplying it with the model continuum flux. As an example, we show in Fig. 7 how we applied the spectral subtraction procedure to TWA 9B.

Since the observed spectra were already flux-calibrated, we analogously derived the flux at Earth ($f_{{\rm obs},i}$) for each line, which was then converted into line luminosity (L_i) and line surface flux using the distances and radii of the objects listed in Table 1. We thus obtained for each star two estimates for $F_{{\rm surf},i}$, one based on the model spectrum flux and one based on the observed flux and the dilution factor, $(R_*/d)^2$. In Fig. 8 we show the good agreement between the fluxes derived in the two ways for the Ca II λ8662 Å line. This confirms that the radii and distances we adopted are realistic. For consistency with the analysis of the other emission lines where no spectral subtraction was necessary, in the remainder of this paper we use for the Ca II IRT the fluxes and derived quantities $f_{{\rm obs},i}$ extracted from the observed spectrum and not from the model (surface) fluxes. These fluxes are summarized in Table 3. In some cases we found no emission above the noise level and the respective fields are empty ("...") in Table 3. Other cases where the equivalent width and flux is consistent with zero within its measurement errors are considered as upper limit.

Following the usual convention, we defined the activity indices as

$$R'_i = \log(L_i/L_{\rm bol}), \quad (1)$$

where i denotes the emission line. The superscript ($'$) indicates that the photospheric contribution has been subtracted from the line flux for features with significant photospheric absorption, that is, in our case for the Ca II IRT.

4. Magnetic activity

4.1. Level of Hα and X-ray activity

For late-type main-sequence stars the chromospheric and coronal activity has long been known to depend on mass, effective

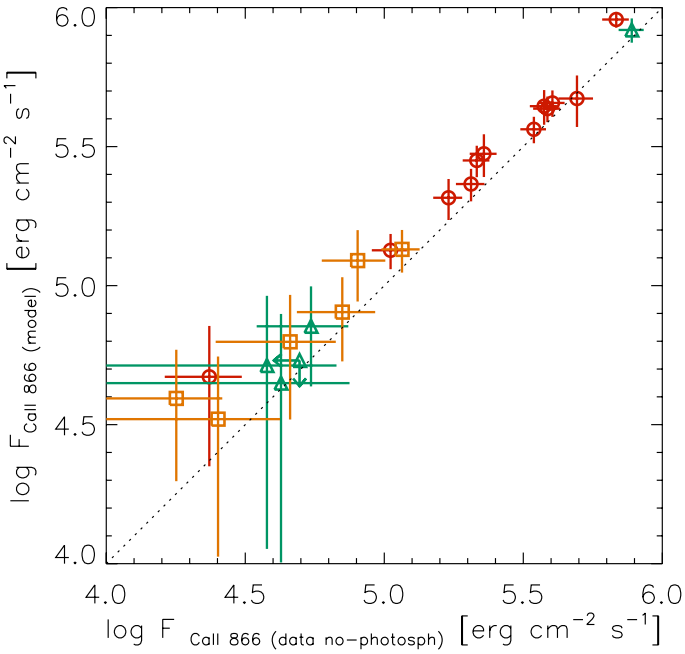

Fig. 8. Comparison between surface flux of the Ca II 8662 Å line computed in two different ways (see text). Same plotting symbols as in Fig. 4.

temperature, and rotation rate (e.g. Wilson 1966; Pallavicini et al. 1981; Noyes et al. 1984). A correlation of activity diagnostics with rotation rate could never firmly be established for PMS stars and, in fact, Preibisch et al. (2005) showed that – primarily due to their long convective turnover times – all PMS stars are in the saturated regime of X-ray activity. The literature is nearly devoid of similar studies on chromospheric Hα emission of PMS stars because the chromospheric contribution of this line is difficult to separate from the effects of accretion and non-accreting PMS samples have received less attention.

In Fig. 9 the Hα and X-ray activity indices of our Class III sample are shown as a function of $T_{\rm eff}$ and are compared with two samples of field M dwarfs. Shown as crosses and plus symbols is the "10-pc sample" of Stelzer et al. (2013), which comprises all M dwarfs within 10 pc of the Sun from the proper motion survey of Lépine & Gaidos (2011). The Hα measurements of these stars have been compiled from the literature by Stelzer et al. (2013), while they extracted the X-ray data from public data archives. Diamonds in the left panel of Fig. 9 refer to the work of Bochanski et al. (2007), who have defined template spectra for the M spectral class from several thousands of Sloan Digital Sky Survey (SDSS) spectra. They distinguished two subgroups of active and inactive stars on the basis of Hα emission and tabulated mean equivalent widths of Balmer lines and the $L_{\rm H\alpha}/L_{\rm bol}$ ratio for the active M0...L0 dwarfs. These mean values for their "active" sample are the ones shown in Fig. 9.

Before comparing field dwarfs and PMS stars, we had to attribute an effective temperature to the field M dwarfs because the mapping between SpT and $T_{\rm eff}$ depends on the evolutionary state of the stars. To this end, we combined the temperature scales of Bessell (1991) and Mohanty & Basri (2003), which together span the full M spectral sequence. Fig. 9 (left panel) shows that for both our PMS sample and the field star sample from Bochanski et al. (2007), $L_{\rm H\alpha}/L_{\rm bol}$ is fairly constant at a similar level of ≈−3.5... − 4.0 up to a temperature of ∼3000 K and drops rapidly toward the end of the M sequence. The plateau for earlier M stars is usually associated with saturation, albeit its origin is

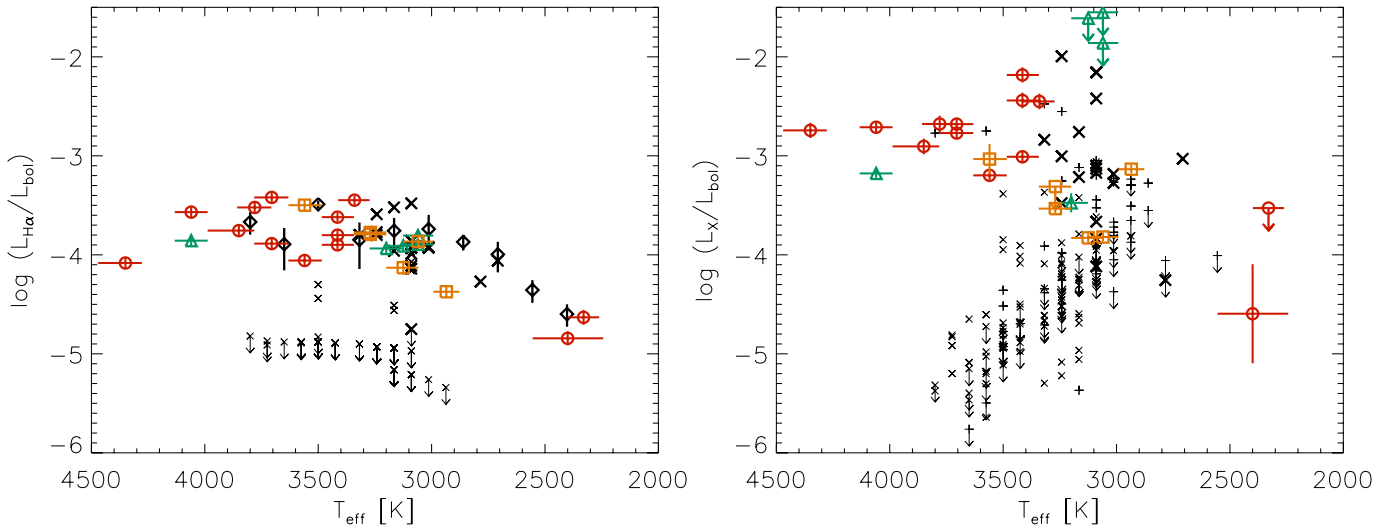

Fig. 9. Hα and X-ray activity index vs effective temperature for the Class III sources (shown with the same plotting symbols as in Fig. 4) compared with two samples of field M dwarfs: for the 10-pc sample from Stelzer et al. (2013) crosses represent stars with measured rotational velocity (small and large symbols for slow and fast rotators, respectively, with dividing line at 3 km s^{-1}) and plus symbols are stars without $v \sin i$ data. The mean active SDSS sample from Bochanski et al. (2007) is represented by diamonds; see Sect. 4.1 for details.

disputed (see e.g. Vilhu & Walter 1987; Doyle 1996; Jardine & Unruh 1999). We found $\langle \log (L_{\mathrm{H}\alpha}/L_{\mathrm{bol}}) \rangle_{\leq \mathrm{M4}} = -3.72 \pm 0.21$ for the mean Hα activity index of the Class III sources with spectral type M4 and earlier, corresponding to $T_{\mathrm{eff}} > 3250$ K. The Hα activity of the 10-pc sample shows a much wider spread for given T_{eff}. This is because, in contrast to the sample from Bochanski et al. (2007), the 10-pc sample comprises many Hα inactive stars displayed as downward pointing arrows in Fig. 9. Moreover, this sample exhibits a range of rotation rates, and these influence the activity level, as can be seen by comparing the large and the small crosses that distinguish stars with $v \sin i \geq 3$ km s^{-1} from those with $v \sin i < 3$ km s^{-1}. Most of the fast-rotating M dwarfs from the 10-pc sample have Hα activity similar to that of the PMS sample which consists entirely of fast rotators. Therefore, although no rotation rates are given by Bochanski et al. (2007), it is likely that their "active" stars are all rapidly rotating.

An analogous graph for the X-ray activity index is shown in the right panel of Fig. 9. For our Class III sample the dependence of the $L_{\mathrm{X}}/L_{\mathrm{bol}}$ ratio on the T_{eff} is equivalent to that of Hα activity, that is, we see a saturation plateau for early-M types that declines for cooler objects. The saturation level is higher in X-rays than in Hα. Analogous to the Hα emission, we computed the mean value for the X-ray activity indices of the Class III sources with SpT M4 and earlier and found $\langle \log (L_{\mathrm{X}}/L_{\mathrm{bol}}) \rangle_{\leq \mathrm{M4}} = -2.85 \pm 0.36$. In the right panel of Fig. 9 the 10-pc sample is again overplotted. The large divergence of the $L_{\mathrm{X}}/L_{\mathrm{bol}}$ level between PMS and field dwarfs seen in the early-M stars is well-known and commonly attributed to rotational evolution and the ensuing decay of activity (e.g. Preibisch & Feigelson 2005). Analogous to the left panel of the same figure, as a proxy for the activity state we highlight stars from the 10-pc sample with $v \sin i > 3$ km s^{-1} with larger crosses. Stars without known rotation rate are marked with a plus symbol. The subsample of fast-rotating field M dwarfs forms the upper boundary and presents $L_{\mathrm{X}}/L_{\mathrm{bol}}$ ratios similar to those of the Class III stars.

We have examined the relation between the activity indices and $v \sin i$ and found no dependence, consistent with the observation that our Class III stars have saturated Hα and X-ray emission and in agreement with previous results in the literature of magnetic activity on PMS stars. Only the two BDs have low activity levels considering their high rotational velocities. Similarly, Reiners & Basri (2010) found in a sample of late-M stars in the field that the fastest rotators show the lowest Hα activity.

4.2. Chromospheric and coronal flux-flux relations

Several previous works have established power-law relationships between pairs of chromospheric emission line fluxes to probe the structure of the outer atmospheres of late-type stars (see e.g. Martínez-Arnáiz et al. 2011, henceforth MA11). While most samples presented in the literature so far regard field stars, we examine here a PMS sample. Similar to previous studies, we fitted relations of the type

$$\log F_1 = c_1 + c_2 \log F_2, \tag{2}$$

where F_i with $i = 1, 2$ are the surface fluxes of two lines, and the coefficients c_1 and c_2 are the free fit parameters. The fits were performed with the least-squares bisector regression described by Isobe et al. (1990). Only stars with detected emission in both diagnostics of the respective flux-flux relation were considered.

The emission lines observed in the X-shooter spectra comprise a wide spectral range. We used here the line fluxes for all Balmer lines up to H11, Ca II H&K, and the two helium lines (He I λ5876 Å and He I λ10830 Å) listed by MTR 13 and our results for the Ca II IRT derived as described in Sect. 3.5. These lines are produced in different layers of the outer atmosphere, from the lower chromosphere to the transition region, as explained in Sect. 1. We also extend our investigation to a comparison between chromospheric and coronal emission using our compilation of X-ray fluxes.

The results of the linear regressions of all examined flux pairs are given in Table 4. Some of the more notable correlations are shown in Figs. 10 and 11. In these two figures the fitted lines are overplotted (dash-dotted and dotted for the uncertainties). Where available, we also show the regressions published previously for different samples of late-type stars (solid lines).

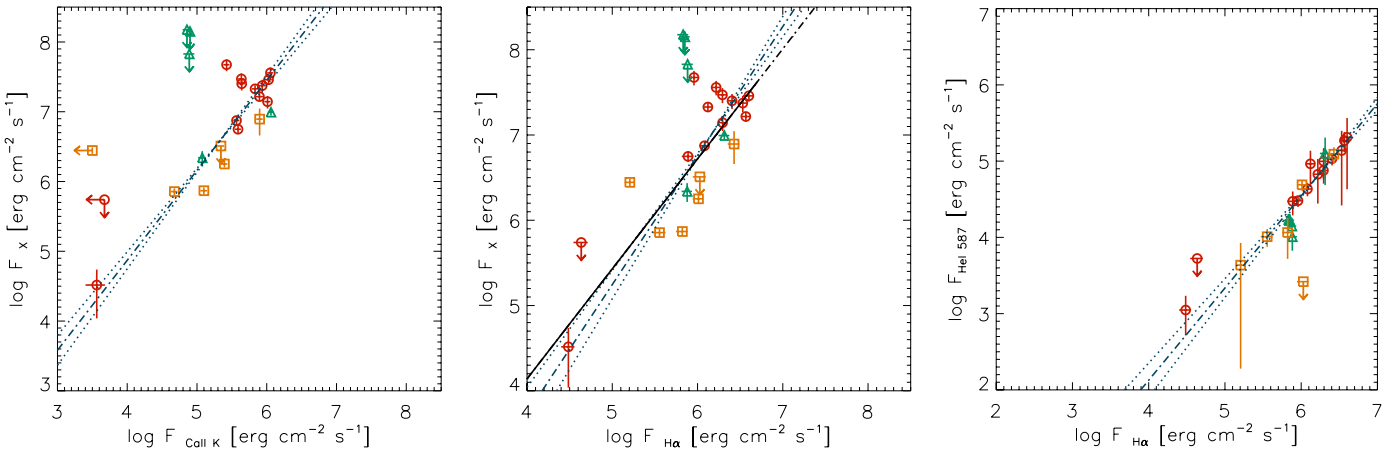

Fig. 10. Flux-flux relations for some of the most often used indicators of chromospheric and coronal activity in M stars (Hα, Ca II K, X-rays and He Iλ 5876 Å). Same plotting symbols as in Fig. 4. The results of a linear regression fit to all detections and its standard deviation are shown as dash-dotted and dotted lines, respectively. For F_X vs. $F_{H\alpha}$ we also show the relation derived in the same way for a sample of field M dwarfs as solid line (see Stelzer et al. 2012a).

For Fig. 10 we selected correlations between some of the most widely used and most easily accessible indicators of magnetic activity (X-rays, Hα, Ca II K, He I λ5876 Å). We compared our results with the relations found in the literature. In particular, the correlation between X-ray and Hα flux has recently been studied by MA11 and by Stelzer et al. (2012a). MA11 considered a sample of nearly 300 single dwarf stars with spectral types from F to mid-M, while Stelzer et al. (2012a) have reanalyzed flux-flux relations for the subsample of M stars from MA11 and combined it with late-M stars. The slope of the F_X vs. $F_{H\alpha}$ relation for our Class III sample is statistically consistent with those of both these studies (see Fig. 10 middle). Moreover, all flux-flux combinations relating the two calcium lines (not shown graphically) agree excellently with the results of MA11.

In Fig. 11 we present the correlations for which MA11 have identified two branches, a main one defined by field stars in a wide range of spectral types (FGKM) and a second one populated by a subsample of M field dwarfs. In the study of MA11 this latter group apparently shows higher Hα and X-ray flux for given Ca II K and Ca IIλ 8498 Å emission. The linear regressions computed by MA11 for the two branches are overplotted as solid black lines in Fig. 11 in the range of fluxes covered by their sample. Evidently, our Class III sample closely follows the upper "active" branch defined by MA11, and it allows us to extend the correlations of Hα vs. Ca II K, Hα vs. Ca IIλ 8498 Å, and X-rays vs. Ca IIλ 8498 Å by 1–2 dex toward lower fluxes. None of the Class III objects is located on the main lower branch occupied by the majority of field stars according to MA11.

Finally, to compare the chromospheric and the coronal radiative output we summed all optical emission lines studied in this paper, that is the Balmer series up to H11, the He I lines at 5876 Å and at 10 830 Å, the three lines of the Ca II IRT, and the Ca II K line. We multiplied the flux of the Ca II K line by a factor of two to approximate the Ca II H emission that was omitted from the observed line list because of its blend with Hϵ. The contribution of Hϵ was approximated as the mean of the observed fluxes of Hδ and H8. The summed chromospheric flux in optical emission lines (F_{opt}) was considered an upper limit if at least one of the examined lines was not detected. The ratios between F_X and F_{opt} are shown in Fig. 12. Stars in which both the X-ray emission and the chromospheric optical emission is an upper limit are not included in Fig. 12 because their corona-to-chromosphere flux ratio is completely unconstrained. In most stars the emission from the corona dominates that from the visible chromosphere. The difference is typically a factor 2 to 5, and there is a possible hint for systematically higher F_X/F_{opt} in TWA members than in those of the younger objects from Lupus and σ Ori.

The full chromospheric radiation budget comprises emission in the near-ultraviolet (NUV) and far-ultraviolet (FUV). Very few records of ultraviolet emission from Class III sources are found in the literature. The *Hubble* Space Telescope (HST) study of Yang et al. (2012) and the Galaxy Evolution Explorer (GALEX) study of Stelzer et al. (2013) have a few stars in common with our X-shooter sample. We list the UV fluxes measured at Earth for these stars in Table 2 together with the sum of the fluxes emitted in the optical emission lines (f_{opt}). The HST fluxes refer to the 1250–1700 Å band, and typically about half of them are emitted in the five strongest emission lines (see Table 4 in Yang et al. 2012). The GALEX FUV and NUV bands comprise 1344–1786 Å and 1771–2831 Å, respectively. The photospheric contribution to the broad-band FUV and NUV fluxes was subtracted by modeling the individual SEDs (see Stelzer et al. 2013). No information on the distribution of the flux on continuum and emission lines is available for the GALEX observations. While a detailed comparison of optical and UV chromospheric emissions is impeded by the small sample size, it seems that the optical contribution dominates.

4.3. Line decrements

Our sample allows us to quantify the relative amount of emission in different parts of the chromosphere for PMS stars throughout the whole M spectral class by means of the observed line flux ratios. Of particular interest are the Balmer decrements (e.g. $f_{H\alpha}/f_{H\beta}$) and the ratio of the Ca II K and Hα flux. We preferred to examine the decrements as a function of T_{eff} instead of SpT because the temperature is a physical parameter, while the SpT is merely an observational proxy of it.

In Fig. 13 we compare flux ratios of the aforementioned emission lines with results for other stars and for the Sun that we retrieved from the literature. In the left panel the observed $f_{H\alpha}/f_{H\beta}$ ratios are shown together with the decrements for the active field M star templates defined by Bochanski et al. (2007),

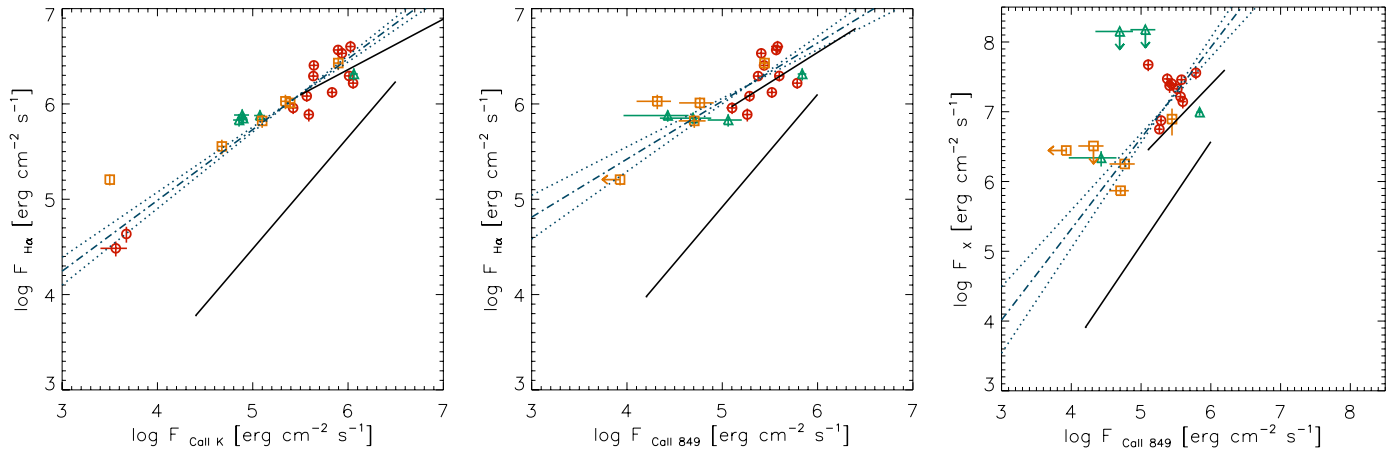

Fig. 11. Flux-flux relations for which MA11 identified two distinct populations in a sample of field stars (shown as solid lines). Our sample of Class III stars is shown with the same plotting symbols as in Fig. 4 and is located on the upper relation. It extends this "active branch" to lower fluxes. Linear regressions and standard deviation for the Class III detections are shown as dash-dotted and dotted lines as in Fig. 10.

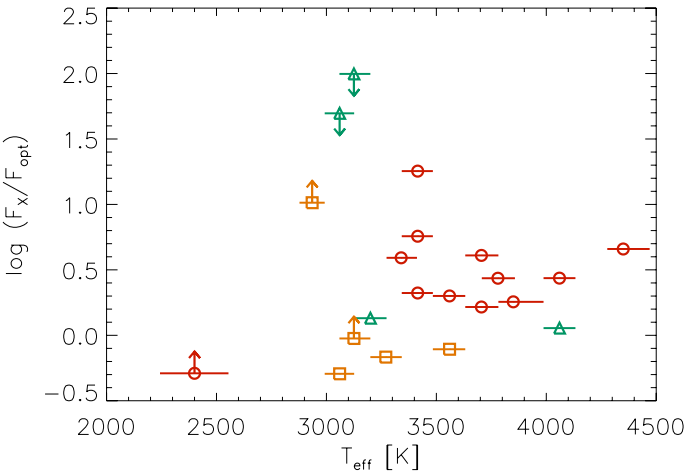

Fig. 12. Logarithm of the ratio between coronal X-ray flux and chromospheric optical flux versus effective temperature. The chromospheric optical flux is defined as the sum of the fluxes of all strong emission lines in the X-shooter spectra. Same plotting symbols as in Fig. 4.

for the M9 field dwarf DENIS-P J104814.7-395606 (henceforth DENIS 1048-3956) derived by Stelzer et al. (2012a) on the basis of an X-shooter spectrum, for the active dM3.5e star AD Leo (see Mauas & Falchi 1994), and for the PMS early-M dwarf AU Mic from Houdebine & Doyle (1994). This last one is particularly relevant because it is a member of the β Pic group with an age of ~12 Myr (Zuckerman et al. 2001; Kalas et al. 2004), similar to the age of the TWA. The typical Hα/Hβ flux ratios of solar prominences and of the solar chromosphere from Tandberg-Hanssen (1967) are also indicated. For both the Class III objects and the field dwarfs, an increase of the Hα/Hβ decrement toward lower $T_{\rm eff}$, that is late-M types, is evident. However, due to the decrease of line fluxes the uncertainties at the end of the M sequence are substantial.

In the right panel of Fig. 13 we show the $f_{\rm Ca\,II\,K}/f_{\rm H\alpha}$ ratio of the Class III sample together with the values observed for DENIS1048-3956 and AD Leo, and the results for the SDSS sample from Bochanski et al. (2007). For this latter one we propagated the errors given by Bochanski et al. (2007), who provided both lines with respect to Hβ. The resulting uncertainties are so large that the line ratios are consistent with zero. The measurements for our Class III sample are more meaningful. The observed Ca II K/Hα ratio of AD Leo is consistent with that of the Class III stars of the same $T_{\rm eff}$. We see a clear trend in our data for decreasing Ca II K versus Hα flux ratio toward lower $T_{\rm eff}$. The difference between the line flux ratio of early-M and late-M stars is much larger for Ca II K/Hα (about a factor six from $T_{\rm eff} \sim 3000$ K to $T_{\rm eff} \sim 4000$ K) than for Hα/Hβ (about a factor two in the same temperature range).

A few features in the behavior of these flux ratios require more detailed investigation. First, the two stars, TWA-6 and TWA-14, stand out from the trend in Fig. 13. They violate the smooth behavior of the flux ratios with spectral type in both panels. For these two objects the Hα line is stronger than expected from their Hβ and Ca II K emission considering the trend of the other stars of similar effective temperature pointing at differences in the structure of their outer atmospheres. Secondly, it is not clear if the trends described above are continuous throughout the lowest effective temperatures ($\lesssim$3000 K). Especially the Ca II K/Hα ratio is sampled by only two PMS BDs, TWA-26 and TWA-29, and by one field ultracool dwarf, DENIS1048-3956 given that the error bars on the SDSS data are prohibitively large.

In Fig. 14 we present the Balmer decrements up to $n = 11$. For clarity, members of the three different SFRs have been given a small horizontal offset with respect to each other. Only stars with detections in the two lines that define the decrement are plotted, and their mean value is shown as a large cross for each energy level n. We chose here to refer the decrements to Hγ because this allows us to compare our observations with results from the literature. The small circles connected with a solid line represent the decrements derived by Houdebine & Doyle (1994) from NLTE radiative transfer modeling of the chromosphere of AU Mic. The observed values for this star are shown as larger filled black circles. An effective temperature of 3500 K and $\log g = 4.75$ were assumed by Houdebine & Doyle (1994) for the photosphere underlying the chromospheric modeling of AU Mic. Therefore, this model can be expected to approximate the chromospheres of our Class III sample, and in particular the TWA members among them. The model of Houdebine & Doyle (1994) somewhat overpredicts their Balmer decrements, but the general agreement is good. A tendency of larger decrements for hotter stars can be seen in Fig. 14. We have highlighted two representatives of the hot and cool end of our sample, SO 879 (K7) and Par-Lup3-2 (M5). A detailed study of the temperature and

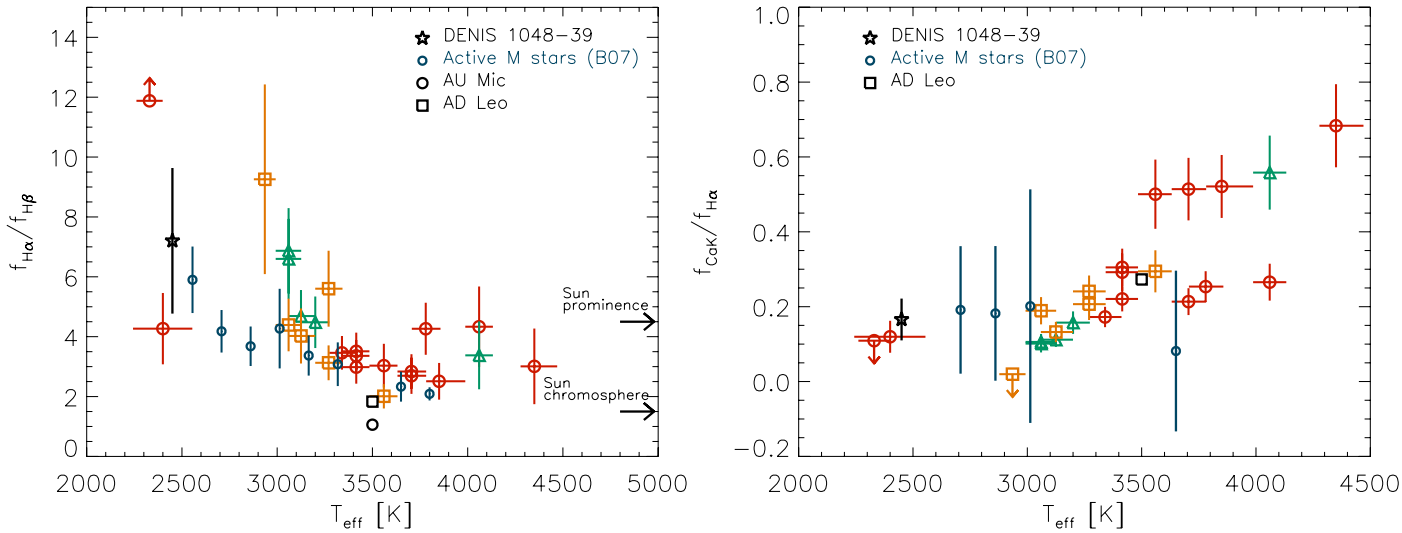

Fig. 13. Chromospheric line flux ratios versus effective temperature: *Left panel* – Hα/Hβ, *right panel* – Ca II K/Hα. Same plotting symbols as in Fig. 4. For comparison we include results for active M dwarf templates from the SDSS (blue circles; Bochanski et al. 2007), the M9 dwarf DENIS 1048-3956 (star symbol; Stelzer et al. 2012a), the PMS M dwarf AU Mic (black circle; Houdebine & Doyle 1994), the M3.5 dwarf AD Leo (black square; Mauas & Falchi 1994), and the Sun (rightward pointing arrows; Tandberg-Hanssen 1967).

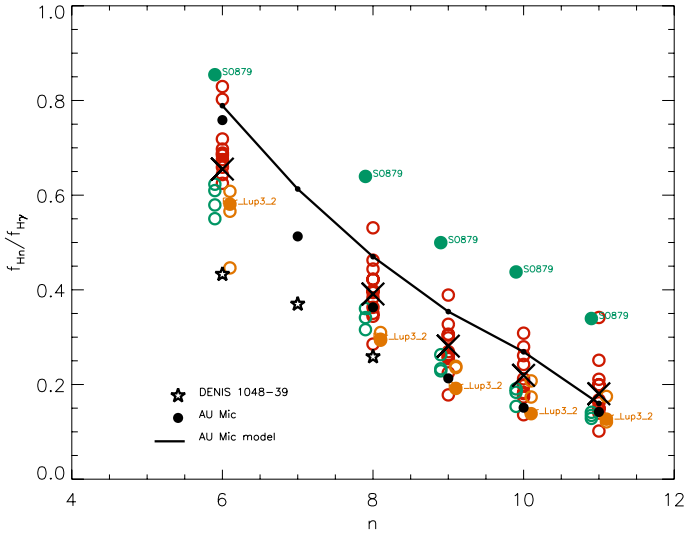

Fig. 14. Balmer decrements with respect to Hγ for all stars from the Class III sample where the two lines comprising the decrement are detected. Same plotting symbols as in Fig. 4. Predicted values from a chromospheric model devised for AU Mic are shown as a solid line, and the observed values of AU Mic are represented by filled black circles.

gravity dependence of the Balmer decrements is deferred to a later point when a grid of NLTE models is available.

5. Summary and conclusions

We have determined the photospheric parameters $T_{\rm eff}$ and $\log g$, rotation velocities, and radial velocities for 24 Class III objects from the TWA, σ Ori, and Lupus III SFRs using the ROTFIT routine to compare X-shooter spectra with synthetic BT-Settl spectra in carefully selected wavelength ranges. The values we found agree excellently with previous measurements given in the literature where available. For four targets in Lupus, all five in σ Ori, and the two coolest of the TWA object(s) we presented the gravity, rotation, and kinematic parameters for the first time. For the remaining two targets in Lupus, Sz 121 and Sz 122, we found a very fast rotation consistent with previous measurements. These two stars are suspected to be spectroscopic binaries.

There are discrepancies between the gravities derived by us from the X-shooter spectra and those predicted by the evolutionary models of Baraffe et al. (1998) and Chabrier et al. (2000). Our findings confirm previous results. In particular, the coolest M-type objects, in our case the two BDs TWA 26 and TWA 29, have a lower gravity than the mid- to early-M stars, a trend that is not present in the models. Mohanty et al. (2004) have discussed problems with the initial conditions, effects of accretion, and the treatment of convection in the evolutionary models as possible causes for this mismatch. The region around $T_{\rm eff} \sim 2500$ K is characterized by the onset of dust formation, and it seems that problems with the dust treatment within the models are responsible for the discrepant gravities across the M spectral sequence in TWA. No evolutionary models are available so far for the latest synthetic atmosphere grid, BT-Settl.

The equivalent widths of the Li Iλ6708 Å line are similar to previous estimates by Mentuch et al. (2008) for the TWA members. No previous reports of lithium exist for the σ Ori and Lupus objects from this sample. The comparison with the curves of growth from the literature (Palla et al. 2007; Zapatero Osorio et al. 2002) yielded a rough estimate for the lithium abundances. We inferred approximate A(Li) $\approx$ 2.5–3.5. Our lithium measurements are thus qualitatively consistent with the young age of the stars.

We measured the activity indices, defined as ratio between the luminosity in the activity diagnostic and the bolometric luminosity, and compared them with those of M dwarfs in the field. For the Class III sources of early-M spectral type the mean activity indices of Hα ($\log(L_{\rm H\alpha}/L_{\rm bol}) = -3.72 \pm 0.21$) and X-rays ($\log(L_{\rm X}/L_{\rm bol}) = -2.85 \pm 0.36$) differ by almost one order of magnitude. Both the absolute values for the mean X-ray and Hα activity indices and the differences between them are similar to those of the active ones among the early-M type field stars presented in the literature (see e.g. Stelzer et al. 2013). "Active" field dwarfs are generally those that rotate faster, which is likely due to relatively young age. Individual ages are generally not available for field dwarfs, but in any case the younger ones among

them are on the order of a few 100 Myr old. Therefore, our finding indicates that in M stars the decline of magnetic activity sets in only after the stars have reached the main-sequence. Similar results have been obtained by Preibisch & Feigelson (2005) in a comparative study of X-ray luminosity functions from the Orion Nebula Cluster (~1 Myr), the Pleiades (~100 Myr), and the Hyades (~600 Myr) cluster, where the authors noted that the decay of activity with age is slower for M stars than for G- and K-type stars. Both the Hα and the X-ray activity index drop sharply for late-M spectral types. Our sample is too small to determine the subtype at which the decline sets in. A similar decrease of Hα and X-ray emission is observed in samples of field stars (e.g. West et al. 2004). It has been ascribed to the increasingly neutral atmospheres of the coolest M dwarfs that impede efficient coupling between matter and magnetic field (Mohanty et al. 2002).

No correlation with rotational velocity is seen in the Class III sample, indicating that the activity of these stars is in the saturated regime, consistent with previous studies of X-ray emission in PMS stars (Preibisch et al. 2005). The situation is less clear for the two BDs, TWA 26 and TWA 29. Their rotational velocities and stellar radii indicate an upper limit to their rotation period of ~8 h. This value is within the range of 4.1 to 88 h for photometrically observed periods of young BDs in the 5 Myr old ϵ Ori cluster (Scholz & Eislöffel 2005). In spite of their evidently fast rotation TWA 26 and TWA 29 have activity levels (in terms of the activity indices) that are at least one order of magnitude lower than those of early-M Class III objects. While the decline of Hα activity index at the cool end of the stellar sequence is well-established for evolved field dwarfs (see e.g. West et al. 2004; Bochanski et al. 2007), the PMS Hα index has to the best of our knowledge not been systematically explored down to the substellar limit. On the X-ray side, even the most sensitive available star-forming region surveys such as the Chandra Orion Ultradeep field (cf. Getman et al. 2005) are barely deep enough for the detection of BD coronae. An X-ray study of the 3 Myr-old cluster IC 348 has yielded a slope steeper than unity for the relation between $L_{\rm x}$ and $L_{\rm bol}$, corresponding to a decrease of the activity index with decreasing luminosity, that is, for cooler objects (Stelzer et al. 2012b). However, the significance of this result is drastically reduced when only Class III sources are considered, suggesting that accretion and not the chromosphere is at the origin of this trend. To summarize, the low activity indices seen in the two Class III BDs of the TWA need to be bolstered with systematic studies of larger samples of young substellar chromospheres. If confirmed, this may indicate that in the substellar regime the dynamo efficiency decouples from the rotation rate, or that some other process such as disruption of the corona by centrifugal forces (Jardine 2004) suppresses the emission.

We estimated the relative contribution of the chromosphere and the corona to the radiative output produced by magnetic activity by comparing the observed fluxes. For the chromosphere the fluxes of all emission lines in the X-shooter spectrum were summed, while for the corona we used the soft X-ray flux. In our sample the X-ray fluxes tend to be higher than the optical radiation measured by the emission lines. Observations extracted from the literature suggest that the UV emission is negligible for the chromospheric radiation budget of these stars, but this has to be corroborated once larger samples of Class III sources have sensitive constraints on their UV fluxes. The spread for the flux ratio $F_{\rm X}/F_{\rm opt}$ is at least one order of magnitude in our Class III sample and a trend for an age dependence of the coronal-to-chromospheric flux ratio is suggested, but requires a larger sample size to be firmly established. Note that the X-ray and optical observations are not simultaneous. The influence of variability, therefore, remains unknown.

Flux-flux relations between individual chromospheric emission lines and those between chromospheric diagnostics and X-ray emission were presented. The results for the Class III stars confirm the existence of the upper "active" branch identified by MA 11 on the basis of a few objects in a large sample of field FGKM stars that deviated from the flux-flux relations of the bulk of objects. As far as we can say considering our sample of 24 Class III sources, all young stars populate this "active" branch. The "active" stars are characterized by a higher ratio between Hα and Ca II emission (both Ca II K and the IRT) than that of the less active ones. Similarly, their X-ray emission is enhanced with respect to Ca II emission. Neither MA11 nor our study found differences in the $F_{\rm H\alpha}$ vs. $F_{\rm X}$ relation for stars from the two branches. Since all these diagnostics are formed in different atmospheric layers, our finding indicates a change in the response of the atmosphere to the drivers of magnetic activity as the activity decreases. This is presumably a consequence of rotational evolution and the ensuing decay of dynamo efficiency. Flux-flux relations for samples known to rotate slowly are needed for a comparison with the very active Class III stars. In particular, it seems that there is a clear distinction between low-activity stars and those with strong Hα and X-ray emission. Given the relation between activity and age, the relative amount of emission in the various diagnostics may, therefore, in the future be applied as a qualitative youth indicator.

Within the spectral class M, the flux ratio between Ca II K and Hα emission shows a significant decrease toward lower $T_{\rm eff}$, while the Hα/Hβ decrements are slightly increasing but are less sensitive to the effective temperature. This may again be a signature of the different layers where these lines form. Two stars deviating from these trends, TWA 6 and TWA 14, are the fastest rotators in our sample. At the same Hβ and Ca II K levels of other stars with similar effective temperature they present higher Hα flux. We conclude that Hα is more sensitive to rotation than other emission lines. This is probably the reason for the existence of the two branches in the flux-flux relations discussed above. No chromospheric model grids are available for the parameter space covered by our Class III sample to be compared with our observations. A dedicated Hα and Ca II study was presented by Houdebine & Stempels (1997) for much less active dM1 stars but no theoretical line fluxes were provided.

The series of Balmer decrements from Hδ to H11 referred to Hγ for our Class III sample are roughly reproduced with the NLTE radiative transfer model devised for the young M dwarf AU Mic by Houdebine & Doyle (1994). The trend is toward smaller decrements for later-M spectral types, analogously to the result for the inverse of Hα/Hβ. Our findings represent a guideline for future chromospheric modeling efforts. Such models should be able to predict the behavior of line flux ratios throughout the whole M spectral class. Moreover, they should explain the emissions of stars with different activity levels.

Acknowledgements. We thank an anonymous referee. J.M.A. and B.S. recognize the active contribution of G.Attusino to some of the teleconferences. We thank the ESO staff for their support during the observations. We also appreciate the support of P. Goldoni, A. Modigliani, and G. Cupani in the use of the X-shooter pipeline.

References

Alcalá, J. M., Stelzer, B., Covino, E., et al. 2011, Astron. Nachr., 332, 242
Allard, F., Homeier, D., & Freytag, B. 2012, ASP Conf. Ser., 448, 91
Baraffe, I., Chabrier, G., Allard, F., & Hauschildt, P. H. 1998, A&A, 337, 403

Barnes, T. G., & Evans, D. S. 1976, MNRAS, 174, 489
Bessell, M. S. 1991, AJ, 101, 662
Beuermann, K., Baraffe, I., & Hauschildt, P. 1999, A&A, 348, 524
Bildsten, L., Brown, E. F., Matzner, C. D., & Ushomirsky, G. 1997, ApJ, 482, 442
Bochanski, J. J., West, A. A., Hawley, S. L., & Covey, K. R. 2007, AJ, 133, 531
Carpenter, J. M. 2001, AJ, 121, 2851
Castro, P. J., Gizis, J. E., & Gagné, M. 2011, ApJ, 736, 67
Chabrier, G., & Küker, M. 2006, A&A, 446, 1027
Chabrier, G., Baraffe, I., Allard, F., & Hauschildt, P. 2000, ApJ, 542, 464
Cody, A. M., & Hillenbrand, L. A. 2010, ApJS, 191, 389
Comerón, F., Fernández, M., Baraffe, I., Neuhäuser, R., & Kaas, A. A. 2003, A&A, 406, 1001
Doyle, J. G. 1996, A&A, 307, L45
Dubath, P., Reipurth, B., & Mayor, M. 1996, A&A, 308, 107
Durney, B. R., De Young, D. S., & Roxburgh, I. W. 1993, Sol. Phys., 145, 207
Fernández, M., Stelzer, B., Henden, A., et al. 2004, A&A, 427, 263
Findeisen, K., & Hillenbrand, L. 2010, AJ, 139, 1338
Franciosini, E., Pallavicini, R., & Sanz-Forcada, J. 2006, A&A, 446, 501
Frasca, A., & Catalano, S. 1994, A&A, 284, 883
Frasca, A., Guillout, P., Marilli, E., et al. 2006, A&A, 454, 301
Getman, K. V., Flaccomio, E., Broos, P. S., et al. 2005, ApJS, 160, 319
Gondoin, P. 2006, A&A, 454, 595
Hernández, J., Hartmann, L., Megeath, T., et al. 2007, ApJ, 662, 1067
Houdebine, E. R. 2011, MNRAS, 411, 2259
Houdebine, E. R., & Doyle, J. G. 1994, A&A, 289, 185
Houdebine, E. R., & Stempels, H. C. 1997, A&A, 326, 1143
Hughes, J., Hartigan, P., Krautter, J., & Kelemen, J. 1994, AJ, 108, 1071
Isobe, T., Feigelson, E. D., Akritas, M. G., & Babu, G. J. 1990, ApJ, 364, 104
Jardine, M. 2004, A&A, 414, L5
Jardine, M., & Unruh, Y. C. 1999, A&A, 346, 883
Kalas, P., Liu, M. C., & Matthews, B. C. 2004, Science, 303, 1990
Kuhi, L. V. 1983, Rev. Mex. Astron. Astrofis., 7, 127
Lawson, W. A., & Crause, L. A. 2005, MNRAS, 357, 1399
Lépine, S., & Gaidos, E. 2011, AJ, 142, 138
López Martí, B., Jiménez-Esteban, F., & Solano, E. 2011, A&A, 529, A108
Luhman, K. L., Stauffer, J. R., Muench, A. A., et al. 2003, ApJ, 593, 1093
Manara, C. F., Testi, L., Rigliaco, E., et al. 2013, A&A, 551, A107
Martínez-Arnáiz, R., López-Santiago, J., Crespo-Chacón, I., & Montes, D. 2011, MNRAS, 414, 2629
Mauas, P. J. D., & Falchi, A. 1994, A&A, 281, 129
Mentuch, E., Brandeker, A., van Kerkwijk, M. H., Jayawardhana, R., & Hauschildt, P. H. 2008, ApJ, 689, 1127
Merín, B., Jørgensen, J., Spezzi, L., et al. 2008, ApJS, 177, 551
Modigliani, A., Goldoni, P., Royer, F., et al. 2010, in SPIE Conf. Ser., 7737
Mohanty, S., & Basri, G. 2003, ApJ, 583, 451
Mohanty, S., Basri, G., Shu, F., Allard, F., & Chabrier, G. 2002, ApJ, 571, 469
Mohanty, S., Basri, G., Jayawardhana, R., et al. 2004, ApJ, 609, 854
Montes, D., & Ramsey, L. W. 1999, in Solar and Stellar Activity: Similarities and Differences, eds. C. J. Butler, & J. G. Doyle, ASP Conf. Ser., 158, 302
Montes, D., de Castro, E., Fernandez-Figueroa, M. J., & Cornide, M. 1995, A&AS, 114, 287
Montes, D., Ramsey, L. W., & Welty, A. D. 1999, ApJS, 123, 283
Neuhäuser, R., Sterzik, M. F., Schmitt, J. H. M. M., Wichmann, R., & Krautter, J. 1995, A&A, 297, 391
Noyes, R. W., Hartmann, L. W., Baliunas, S. L., Duncan, D. K., & Vaughan, A. H. 1984, ApJ, 279, 763
Palla, F., Randich, S., Pavlenko, Y. V., Flaccomio, E., & Pallavicini, R. 2007, ApJ, 659, L41
Pallavicini, R., Golub, L., Rosner, R., et al. 1981, ApJ, 248, 279
Parker, E. N. 1993, ApJ, 408, 707
Pecaut, M. J., Mamajek, E. E., & Bubar, E. J. 2012, ApJ, 746, 154
Preibisch, T., & Feigelson, E. D. 2005, ApJS, 160, 390
Preibisch, T., Kim, Y.-C., Favata, F., et al. 2005, ApJS, 160, 401
Reiners, A., & Basri, G. 2010, ApJ, 710, 924
Rutten, R. J. 2007, in The Physics of Chromospheric Plasmas, eds. P. Heinzel, I. Dorotovič, & R. J. Rutten, ASP Conf. Ser., 368, 27
Sacco, G. G., Franciosini, E., Randich, S., & Pallavicini, R. 2008, A&A, 488, 167
Schneider, A., Melis, C., & Song, I. 2012, ApJ, 754, 39
Scholz, A., & Eislöffel, J. 2005, A&A, 429, 1007
Scholz, A., Coffey, J., Brandeker, A., & Jayawardhana, R. 2007, ApJ, 662, 1254
Shkolnik, E. L., Liu, M. C., Reid, I. N., Dupuy, T., & Weinberger, A. J. 2011, ApJ, 727, 6
Stelzer, B., Scholz, A., & Jayawardhana, R. 2007, ApJ, 671, 842
Stelzer, B., Alcalá, J., Biazzo, K., et al. 2012a, A&A, 537, A94
Stelzer, B., Preibisch, T., Alexander, F., et al. 2012b, A&A, 537, A135
Stelzer, B., Marino, A., Micela, G., López-Santiago, J., & Liefke, C. 2013, MNRAS, 431, 2063
Tandberg-Hanssen, E. 1967, Solar activity (Waltham, Mass: Blaisdell)
Taylor, M. B. 2005, in Astronomical Data Analysis Software and Systems XIV, eds. P. Shopbell, M. Britton, & R. Ebert, ASP Conf. Ser., 347, 29
Vaiana, G. S., & Sciortino, S. 1987, in Circumstellar Matter, eds. I. Appenzeller & C. Jordan, IAU Symp., 122, 333
Vernazza, J. E., Avrett, E. H., & Loeser, R. 1981, ApJS, 45, 635
Vilhu, O., & Walter, F. M. 1987, ApJ, 321, 958
Voges, W., Aschenbach, B., Boller, T., et al. 1999, A&A, 349, 389
Voges, W., Aschenbach, B., Boller, T., et al. 2000, VizieR Online Data Catalog, IX/29
Walkowicz, L. M., Johns-Krull, C. M., & Hawley, S. L. 2008, ApJ, 677, 593
Walter, F. M. 1986, ApJ, 306, 573
Walter, F. M., Sherry, W. H., Wolk, S. J., & Adams, N. R. 2008, The σ Orionis Cluster, ed. B. Reipurth, 732
Welty, A. D., & Ramsey, L. W. 1995, AJ, 110, 336
West, A. A., Hawley, S. L., Walkowicz, L. M., et al. 2004, AJ, 128, 426
White, R. J., & Basri, G. 2003, ApJ, 582, 1109
Wichmann, R., Covino, E., Alcalá, J. M., et al. 1999, MNRAS, 307, 909
Wilson, O. C. 1966, ApJ, 144, 695
Yang, H., Herczeg, G. J., Linsky, J. L., et al. 2012, ApJ, 744, 121
Zapatero Osorio, M. R., Béjar, V. J. S., Pavlenko, Y., et al. 2002, A&A, 384, 937
Zuckerman, B., & Song, I. 2004, ARA&A, 42, 685
Zuckerman, B., Song, I., Bessell, M. S., & Webb, R. A. 2001, ApJ, 562, L87

Pages 15 to 16 are available in the electronic edition of the journal at http://www.aanda.org

Table 2. Coronal and chromospheric fluxes.

Name	log f_X [erg/cm^2/s]		Ref.	log f_{opt} [erg/cm^2/s]	log $f_{FUV,HST}$ [erg/cm^2/s]	log $f_{FUV,GALEX}$ [erg/cm^2/s]	log $f_{NUV,GALEX}$ [erg/cm^2/s]
TWA 9A	−11.51	[−11.61, −11.44]		−12.17	−12.85	...	...
SO 879	−13.08	[−13.13, −13.03]	(1)	−13.13	...	...	...
TWA 6	−11.58	[−11.65, −11.52]		−12.02	−12.57	...	...
TWA 25	−11.47	[−11.57, −11.40]		−11.73	...	...	...
TWA 14	−11.97	[−12.07, −11.88]		−12.40	...	−12.32	−12.57
TWA 13B	−11.42	[−11.48, −11.37]		−12.03	−12.91	−12.68	−12.64
TWA 13A	−11.42	[−11.48, −11.37]		−11.63	−12.89	−12.68	−12.64
TWA 2A	−11.52	[−11.58, −11.46]		−11.82	...	−12.82	−12.71
Sz 122	−12.73	[−12.96, −12.58]		−12.62	...	...	...
TWA 9B	−11.51	[−11.61, −11.44]		−12.77	−13.84	...	...
TWA 15B	−11.99	[−12.08, −11.91]		−12.74	...	...	...
TWA 7	−11.54	[−11.60, −11.48]		−11.86	−12.58	...	...
TWA 15A	−11.99	[−12.08, −11.91]		−12.58	...	...	...
Sz 121	<−12.75			<−12.94	...	...	...
Sz 94	−13.39	[−13.44, −13.35]	(2)	−13.22	...	...	...
SO 797	−14.34	[−14.47, −14.25]	(1)	−14.47	...	...	...
SO 641	<−12.75			−14.75	...	...	...
Par-Lup3-2	−13.68	[−13.73, −13.63]	(2)	<−13.65	...	...	...
SO 925	<−12.75			<−14.81	...	...	...
SO 999	<−12.75			−14.44	...	...	...
Sz 107	−13.71	[−13.76, −13.66]	(2)	−13.41	...	...	...
Par-Lup3-1	−13.41	[−13.46, −13.37]	(2)	<−14.43	...	...	...
TWA 26	−15.25	[−15.73, −15.03]	(3)	<−14.96	...	...	...
TWA 29	<−14.63		(4)	<−15.29	...	...	...

Notes. X-ray fluxes (f_X) and upper/lower bounds with references from the literature (see Sect. 2.2). Optical chromospheric flux (f_{opt}) from the sum of the emission lines in the X-shooter spectra. FUV and NUV fluxes from the literature (see Sect. 4.2).

References. (1) − Franciosini et al. (2006); (2) − Gondoin (2006); (3) − Castro et al. (2011); (4) − Stelzer et al. (2007).

Table 3. Equivalent widths and fluxes of Ca II IRT.

Name	W_{8498} [mÅ]	log f_{8498} [erg/cm^2/s]		W_{8542} [mÅ]	log f_{8542} [erg/cm^2/s]		W_{8662} [mÅ]	log f_{8662} [erg/cm^2/s]	
TWA 9A	500 ± 13	−13.28	[−13.33, −13.24]	659 ± 22	−13.16	[−13.21, −13.12]	558 ± 25	−13.24	[−13.29, −13.19]
SO 879	618 ± 16	−14.23	[−14.28, −14.19]	806 ± 18	−14.11	[−14.16, −14.07]	696 ± 18	−14.18	[−14.23, −14.14]
TWA 6	355 ± 38	−13.46	[−13.53, −13.40]	402 ± 35	−13.33	[−13.39, −13.27]	384 ± 39	−13.35	[−13.41, −13.29]
TWA 25	477 ± 15	−13.02	[−13.07, −12.98]	590 ± 19	−12.93	[−12.98, −12.89]	484 ± 16	−13.01	[−13.06, −12.97]
TWA 14	397 ± 22	−13.93	[−13.99, −13.89]	586 ± 23	−13.68	[−13.73, −13.64]	485 ± 24	−13.77	[−13.82, −13.72]
TWA 13B	412 ± 15	−13.22	[−13.27, −13.18]	506 ± 17	−13.14	[−13.18, −13.09]	429 ± 15	−13.21	[−13.26, −13.16]
TWA 13A	491 ± 19	−13.07	[−13.12, −13.02]	640 ± 26	−12.95	[−13.00, −12.91]	515 ± 26	−13.05	[−13.10, −13.00]
TWA 2A	317 ± 18	−13.00	[−13.06, −12.96]	366 ± 16	−12.94	[−12.99, −12.90]	295 ± 19	−13.03	[−13.09, −12.99]
Sz 122	465 ± 34	−14.18	[−14.24, −14.13]	295 ± 36	−14.38	[−14.45, −14.32]	194 ± 23	−14.56	[−14.63, −14.50]
TWA 9B	296 ± 23	−14.08	[−14.14, −14.03]	293 ± 23	−14.09	[−14.15, −14.04]	246 ± 26	−14.16	[−14.23, −14.11]
TWA 15B	524 ± 23	−14.08	[−14.13, −14.04]	619 ± 22	−14.01	[−14.06, −13.97]	474 ± 22	−14.12	[−14.18, −14.08]
TWA 7	440 ± 22	−13.13	[−13.18, −13.08]	491 ± 24	−13.00	[−13.05, −12.95]	389 ± 24	−13.10	[−13.16, −13.05]
TWA 15A	652 ± 33	−13.95	[−14.00, −13.90]	703 ± 26	−13.92	[−13.97, −13.87]	541 ± 26	−14.03	[−14.08, −13.98]
Sz 121	65 ± 25	−14.94	[−15.16, −14.80]	109 ± 43	−14.72	[−14.94, −14.57]	250 ± 59	−14.35	[−14.48, −14.25]
Sz 94	151 ± 57	−14.88	[−15.09, −14.73]	132 ± 54	−14.93	[−15.17, −14.78]	183 ± 54	−14.79	[−14.96, −14.67]
SO 797	71 ± 46	−16.25	[−16.72, −16.03]	332 ± 71	−15.58	[−15.70, −15.49]	144 ± 50	−15.95	[−16.14, −15.81]
SO 641	153 ± 83	−16.21	[−16.55, −16.01]	239 ± 106	−16.01	[−16.27, −15.85]	117 ± 91	−16.32	[−16.98, −16.07]
Par-Lup3-2	...	...		<203	−14.83		102 ± 68	−15.13	[−15.61, −14.91]
SO 925	343 ± 129	−15.86	[−16.08, −15.72]	<202	−16.09		<148	−16.23	
SO 999	...	...		294 ± 160	−15.58	[−15.93, −15.39]	126 ± 96	−15.95	[−16.58, −15.70]
Sz 107	234 ± 70	−14.87	[−15.03, −14.75]	235 ± 95	−14.87	[−15.10, −14.72]	211 ± 95	−14.91	[−15.18, −14.75]
Par-Lup3-1	<107	−15.93		<158	−15.76		225 ± 102	−15.60	[−15.88, −15.44]
TWA 26	...	...		...	...		...	...	
TWA 29	...	...		...	...		1096 ± 320	−16.00	[−16.16, −15.88]

Table 4. Linear fit coefficients for flux-flux relationships of type $\log F_1 = c_1 + c_2 \log F_2$.

Line 1	Line 2	N_*	c_1	c_2
Hβ	Hα	23	-1.71 ± 0.56	1.19 ± 0.09
Hγ	Hα	23	-1.96 ± 0.70	1.18 ± 0.11
Hδ	Hα	23	-2.43 ± 0.97	1.23 ± 0.16
H8	Hα	21	-2.37 ± 0.94	1.19 ± 0.15
H9	Hα	20	-4.81 ± 1.03	1.56 ± 0.17
H10	Hα	20	-5.31 ± 1.06	1.62 ± 0.18
H11	Hα	20	-5.42 ± 1.01	1.62 ± 0.17
Hγ	Hβ	23	-0.25 ± 0.18	1.00 ± 0.03
Hδ	Hβ	23	-0.66 ± 0.33	1.04 ± 0.06
He I 587	Hα	23	-2.77 ± 0.69	1.22 ± 0.11
He I 1083	Hα	6	-2.94 ± 2.44	1.32 ± 0.38
Hα	Ca II K	23	$+2.35 \pm 0.45$	0.69 ± 0.08
Hα	Ca II849	19	$+2.95 \pm 0.52$	0.62 ± 0.10
Hα	Ca II854	19	$+2.72 \pm 0.51$	0.65 ± 0.10
Hα	Ca II866	22	$+1.31 \pm 0.90$	0.92 ± 0.17
He I 587	Ca II K	23	$+0.08 \pm 0.40$	0.83 ± 0.07
Ca II K	Ca II849	19	$+0.89 \pm 0.76$	0.90 ± 0.14
He I 587	Ca II849	19	-0.10 ± 0.59	0.92 ± 0.11
Ca II 849	Ca II854	18	-0.58 ± 0.59	1.09 ± 0.10
Ca II 849	Ca II866	18	-0.68 ± 0.71	1.12 ± 0.13
Xrays	Hα	19	-2.27 ± 0.83	1.50 ± 0.14
Xrays	CaIIK	19	$+1.04 \pm 1.01$	1.06 ± 0.17
Xrays	CaII 849	16	$+0.21 \pm 1.09$	1.28 ± 0.20
He I 587	Xrays	17	$+1.65 \pm 0.84$	1.10 ± 0.17

Notes. "N_*" is the number of stars detected in both lines.